

OBSERVATIONS OF CHEMICALLY ENRICHED QSO ABSORBERS NEAR $Z \sim 2.3$ GALAXIES: GALAXY-FORMATION FEEDBACK SIGNATURES IN THE IGM¹

ROBERT A. SIMCOE^{2,3}, WALLACE L.W. SARGENT⁴, MICHAEL RAUCH⁵, GEORGE BECKER⁴

Draft version September 17, 2018

ABSTRACT

We present a comparative study of galaxies and intergalactic gas toward the $z = 2.73$ quasar HS1700+6416, to explore the effects of galaxy formation feedback on the IGM. Our observations and ionization simulations indicate that the volume within $100 - 200h_{71}^{-1}$ physical kpc of high-redshift galaxies is populated by very small ($\Delta L \lesssim 1$ kpc), dense ($\rho/\bar{\rho} \sim 1000$), and metal-rich ($Z \gtrsim \frac{1}{10} - \frac{1}{3}Z_{\odot}$) absorption-line regions. These systems often contain shock-heated gas seen in O VI, and may exhibit [Si/C] abundance enhancements suggestive of preferential enrichment by Type II supernovae. We argue that the absorber geometries resemble thin sheets or bubbles, and that their unusual physical properties can be explained using a simple model of radiatively efficient shocks plowing through moderately overdense intergalactic filaments. The high metallicities suggest that these shocks are being expelled from—rather than falling into—star forming galaxies. There is a dropoff in the intergalactic gas density at galaxy impact parameters of $\gtrsim 300$ physical kpc ($\gtrsim 1$ comoving Mpc) that may represent boundaries of the gas structures where galaxies reside. The heavy-element enhancement near galaxies covers smaller distances: at galactocentric radii between $100 - 200h_{71}^{-1}$ kpc the observed abundances blend into the general metallicity field of the IGM. Our results suggest that either supernova-driven winds or dynamical stripping of interstellar gas alters the IGM near massive galaxies, even at $R \gtrsim 100$ kpc. However, only a few percent of the total mass in the Ly- α forest is encompassed by this active feedback at $z \sim 2.5$. The effects could be more widespread if the more numerous metal-poor C IV systems at impact parameters $\gtrsim 200h_{71}^{-1}$ kpc are the tepid remnants of very powerful late-time winds. However, based on present observations it is not clear that this scenario is to be favored over one involving pre-enrichment by smaller galaxies at $z \gtrsim 6$.

Subject headings: cosmology:miscellaneous - galaxies:formation - intergalactic medium - quasars:absorption lines - galaxies:feedback

1. INTRODUCTION

A wealth of evidence suggests that early galaxies expelled chemically enriched gas widely into their surroundings. This material may have been thrown off by shocks or tidal interactions as proto-galactic clumps collided, formed stars, and merged into larger units (Gnedin 1998; Cox et al. 2004). Or, the feedback may have been powered by supernovae in the star forming regions themselves (e.g., Mac Low & McCray 1988). Whatever the mechanism, these early galaxy/IGM interactions must have been much more vigorous than we observe in the present day.

Starburst galaxies are often accompanied by supernova-driven outflows which can carry enriched material over intergalactic distances (Lehnert & Heckman 1996). At low redshift, these so-called superwinds preferentially occur in dwarf galaxies whose halo escape velocities are small (e.g., Heckman et al. 2001;

Martin et al. 2002). At high redshift, the star formation density was much higher, so the corresponding increase in supernova frequency should allow larger galaxies to drive superwinds. This phenomenon is indeed seen in $z \gtrsim 3$ galaxies, most of which bear the spectroscopic signature of metal-rich outflows (Franx et al. 1997; Pettini et al. 2001).

Ultimately, any feedback theory must explain how the IGM was populated with heavy elements from very early times. No decline is observed in the C IV contribution to closure density out to redshift $z \gtrsim 5$ (Pettini et al. 2003; Songaila 2001). Moreover by $z \sim 2-3$, C IV and O VI can be observed in gas with density near the cosmic mean (Simcoe et al. 2004; Schaye et al. 2003; Aguirre et al. 2003). From the observed abundances, one infers that within the first 15% of the Hubble time, $\sim 50\%$ of all baryons (i.e., most of the cosmic filaments) were mixed with chemically-rich gas. To produce the observed abundances, the average galaxy at $z \gtrsim 2.5$ would need to eject $\gtrsim 15\%$ of its manufactured metals into the IGM (Simcoe et al. 2004).

A relationship between high-redshift galactic winds and the observed intergalactic abundances has long been postulated, yet relatively few details are known about how the winds' chemicals and energy physically mix over large scales. Adelberger et al. (2003, 2005a) have studied the large-scale cross-correlation between $z \sim 2-3$ Lyman break galaxies, Ly- α forest lines, and C IV systems. They found a positive correlation between galaxies and C IV systems extending over $4.2h_{71}^{-1}$ comoving Mpc.

¹ Includes observations made at the W.M. Keck Observatory, which is operated as a scientific partnership between the California Institute of Technology and the University of California; it was made possible by the generous support of the W.M. Keck Foundation.

² MIT Center for Space Research, 77 Massachusetts Ave. #37-664B, Cambridge, MA 02139, USA; simcoe@mit.edu

³ Pappalardo Fellow in Physics

⁴ Palomar Observatory, California Institute of Technology, Pasadena, CA 91125, USA; wws@astro.caltech.edu, gdb@astro.caltech.edu

⁵ Carnegie Observatories, 813 Santa Barbara Street, Pasadena, CA 91101, USA; mr@ociw.edu

Moreover the strongest C IV absorbers correlate more strongly with galaxies than galaxies do with each other. This suggests that these “strong” C IV systems (roughly $N_{\text{C IV}} \gtrsim 10^{13}$) congregate directly around individual galaxy haloes. They interpret the galaxy-C IV clustering as a signature of late superwinds, but similar analyses at low redshift (Chen et al. 2001) and at high redshift using quasar spectra alone (Rauch et al. 1997a) find that the same observations can be explained by accretion of pre-enriched gas during hierarchical galaxy assembly (see also, Porciani & Madau 2005).

At $z \sim 2.5$, high column density C IV systems are often accompanied by strong O VI absorption, as would be found in hot ($T \gtrsim 10^5$), shock-heated environments (Simcoe et al. 2002). Typically these absorbers are marginally optically thin ($N_{\text{H I}} \sim 10^{15} - 10^{16.5}$), but they display a very rich chemical structure, containing many heavy elements in a broad range of temperatures and ionization states. The strong association between C IV systems and galaxies at higher redshift, the presence of shock-heating, and the apparently strong metal enrichment together suggest that the strongest O VI and C IV systems trace late stages of galaxy feedback, where chemicals and energy mix into the IGM in real-time. Very recent reports of a strong correlation between galaxies and O VI absorption lend further support to this hypothesis (Adelberger et al. 2005a).

In this paper, we dissect the physical properties of six metal-rich absorption line systems, and examine their relationship with nearby star-forming galaxies. The systems are primarily selected for O VI absorption, but supplemented by one N V and one Mg II identification. Redshifts near $z \sim 2.5$ are particularly convenient for these investigations, from the perspective of both the absorbers and the galaxies. A host of important rest-frame UV lines which vary widely in ionization potential can be observed at optical wavelengths from the ground. This enables us to study intergalactic absorption systems in physical states ranging from hot and collisionally ionized (O VI, N V), to warm and photoionized (Si IV, C IV), to cool and nearly neutral (Fe II, Mg II, Al II). Also, broadband color-selection techniques are efficient at isolating $z \sim 2.5$ galaxies (Steidel et al. 2004). Galaxy samples reaching the equivalent of L^* and below may be assembled using reasonable multislit integrations with 6-10m class telescopes.

Our preliminary investigations are based upon six absorption systems and 14 galaxies towards a single quasar sightline. We construct detailed component-by-component ionization models of the absorbers, using their full complement of heavy-element transitions to constrain gas densities, metallicities, [Si/C] abundance enhancements, sizes, and temperatures. These properties are examined in light of each systems’ stellar neighborhood, which is charted using color selected, spectroscopically confirmed high redshift galaxies. In Section 2 we describe the observational program, followed by a discussion of our absorption line fits and ionization simulations in Sections 3 and 4. In Section 5 we demonstrate how the absorption line properties are naturally explained by a generic model of a radiative shocks propagating into cosmic filaments. Finally, in Section 6 we elaborate on the connection between high-metallicity absorbers and nearby galaxies, and comment on the signif-

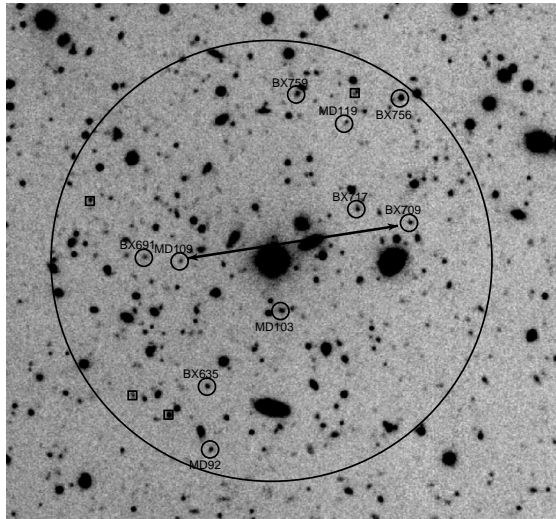


FIG. 1.— G band image of HS1700+6416 field. Spectroscopically identified $z \sim 1.8 - 2.7$ galaxies are labeled with circles (See Table 1 for galaxy properties). Unconfirmed photometric candidates are indicated with square boxes. The large circle indicates an impact parameter of $500h_{71}^{-1}$ physical kpc from the QSO line of sight at $z = 2.4$; the radial limit of the sample. MD109 and BX709 have very similar redshifts ($z = 2.285, 2.2942$) and may be related to a single-component C IV system at $z = 2.28956$ (See Section 6.2). The faintest objects in the image have $G \approx 28$; accordingly the $R < 25.5$ sample limit is dictated by spectroscopic rather than photometric sensitivities. Image provided courtesy of C. Steidel.

icance of galaxy feedback in a cosmological context.

2. DATA AND OBSERVATIONS

Our observations are centered upon the $z = 2.73$ QSO HS1700+6416 (Reimers et al. 1989). We first observed HS1700 with HIRES in April 2001 as part of a multi-sightline survey for intergalactic O VI absorption (Simcoe et al. 2002).

HS1700 is very bright ($V \sim 16.1$) and it is one of only a few objects suitable for studying the He II Ly- α forest at $z \sim 2.5 - 3.0$. Accordingly, it has been observed extensively from the ground (Tripp et al. 1997), and also from space using FOS (Vogel & Reimers 1995) and FUSE (Reimers et al. 2004). These authors have all noted the presence of several near-Lyman-limit systems along the line of sight, which are optically thin yet exhibit high apparent metallicities. To investigate these systems in greater detail, we have obtained high signal-to-noise ratio HIRES spectra with coverage from 3200\AA to nearly $1\mu\text{m}$. This enables measurements of a large host of ion transitions for systems in the $1.8 \lesssim z \lesssim 2.8$ range. In the full sample, we have observed lines from H I, C II, C III, C IV, Si II, Si III, Si IV, O VI, N II, N V, Al II, Mg II, and Fe II. This list covers a wide range of ionization potentials, providing considerable leverage for our ionization models.

2.1. Galaxy Observations

Recently the HS1700 field has also been targeted as part of a $z \sim 1.4 - 2.5$ galaxy survey by Steidel et al. (2004). The authors compiled lists of candidate objects from deep, wide-field U_n, G, R broadband images, using the “BX” and “MD” color selection criteria outlined in Adelberger et al. (2004). They obtained spectroscopic

redshifts for ~ 100 candidates using Keck/LRIS-B. These galaxies’ colors and redshifts were kindly provided to us by C. Steidel. We focus on a small subset of the total galaxy sample, containing objects with impact parameters $\rho < 500h_{71}^{-1}$ kpc (physical) from the QSO sightline⁶.

Fourteen photometric candidates meet this criterion, and their properties are summarized in Table 1. Ten of these galaxies have been observed successfully for redshifts, three have been attempted unsuccessfully, and one has not been attempted. The redshift identifications are 100% complete for photometric candidates at $R < 25.5$, within $\sim 400h_{71}^{-1}$ physical kpc of the QSO sightline. However, the photometric parent sample is probably only $\sim 50 - 60\%$ complete at these redshifts because of object blending or noise, or because some $z \sim 2.3$ galaxies fall outside of the color selection boundaries (C. Steidel, private communication).

Figure 1 presents a summary image of the field, with the relative locations of the QSO and $z \sim 2.5$ galaxies. The large circle shows the approximate $500h_{71}^{-1}$ kpc sample boundary; small circles indicate objects with confirmed redshifts, and unconfirmed photometric candidates are indicated with squares. We are primarily interested in foreground galaxy/absorber systems, so we have omitted galaxies with $z \geq 2.7$, which are close to the QSO’s emission redshift ($z_{QSO} = 2.73$). The galaxy statistics in this environment could be biased by clustering around the QSO, and the absorption systems would be subject to a locally anomalous radiation field.

The photometric limit of the candidate sample is $R < 25.5$, corresponding to $M_{2000\text{\AA}}^{\circ} = -20.8$ at $z \sim 2.3$. It is not entirely straightforward to relate this to a luminosity function due to evolutionary and bandpass effects. However, to provide some context we note that for R band observations of $z \sim 3$ galaxies (corresponding to 1700\AA in the rest-frame), $m_{(z=3)}^* = 24.48$ (Steidel et al. 1999). At $z \sim 2.3$, this translates to $m_{(z=2.3)}^* = 24.0$ at $\lambda_{\text{rest}} \approx 2000\text{\AA}$ using a naive scaling which accounts simply for luminosity distance. By this measure the luminosity cutoff of the HS1700 galaxy sample is $\sim \frac{1}{4}L^*$. The true cutoff could be slightly brighter due to downward evolution of the luminosity function between $z \sim 3$ and $z \sim 2.5$ ($\Delta m \sim 0.2 - 0.3$, Arnouts 2004) or color differences from 1700\AA to 2000\AA . However, early compilations of galaxy samples in our redshift range find a nearly identical luminosity function at $z \sim 3$ and $z \sim 2.2$ (Reddy et al. 2005).

Erb et al. (2003) have also obtained K band spectra of the four sample galaxies nearest the quasar sightline (indicated in Table 1). These data cover the $H\alpha$ transition, whose emission line is a much more reliable estimate of the galaxies’ stellar redshift than rest-frame UV lines (which are often offset from the true systemic redshift). Much of our analysis concerns these closest systems, and we adopt Erb’s $H\alpha$ redshifts where possible. We also quote the star formation rates derived from their $H\alpha$ observations. Finally, Table 1 also lists stellar mass estimates for each galaxy, based upon stellar pop-

ulation models that incorporate rest-frame UV through near-IR photometry (Shapley et al. 2005).

2.2. HIRES Observations

We observed HS1700+6416 with HIRES on several different occasions, using different instrument configurations to capture transitions ranging from the very blue (O VI , N V) to the very red (Fe II , Mg II). All spectra were obtained through an 0.86 arcsecond slit, which corresponds to a velocity resolution of $\Delta v = 6.6$ km/s (FWHM). We extracted 2-D echelle spectra using T. Barlow’s MAKEE reduction package, fit cubic spline continua to each echelle order, and divided the data by the model continuum. Finally, the unity normalized spectra were rebinned onto constant velocity pixels and the orders were combined to produce a single, nearly continuous spectrum ranging from $3200\text{\AA} - 1\mu\text{m}$ (there is a coverage gap in the $6200 - 7300\text{\AA}$ range which is sparsely populated by $z \sim 2.5$ ions). Our continuum determination should be quite accurate in regions redward of the QSO’s Ly- α emission line, with errors probably below $\lesssim 0.5 - 1\%$ because of the data’s high signal to noise. Within the Ly- α forest the errors are difficult to estimate. There are still numerous portions of clean spectrum that could be used to constrain the shape of the spline, but in some heavily blended regions the errors could possibly amount to $5 - 10\%$.

We searched the 1-D spectrum visually for highly ionized absorption systems, which were identified via O VI and/or N V doublets. Both these transitions are blended amongst H I lines from the Ly- α and Ly- β forests, which considerably complicates their identification. To improve our success rate, we adopted the procedure of Carswell et al. (2002), fitting absorption profiles to the entire Ly- α forest and using these parameters to remove the absorption signatures of the corresponding Ly- β and higher order lines. A search of the “cleaned” spectrum for O VI and N V absorption yielded five clear detections—four identified from O VI , and one from N V . The one system identified via N V is located at $z = 1.84$, where O VI cannot be observed from the ground due to the atmospheric UV cutoff.

In addition to these five systems, we found a sixth example that appeared to be quite metal rich, based upon the detection of C IV , C II , Si II , Si III , Si IV , and Mg II . All six systems are accompanied by C IV absorption with $N_{C\text{IV}} > 10^{13}$, which puts them in league with the strong C IV systems that cluster strikingly with galaxies at $z \sim 3$ (Adelberger et al. 2003, 2005a). They also exhibit strong, sub-Lyman-limit H I absorption ($N_{H\text{I}} \sim 10^{15-16}$), and a rich assortment of lower ionization potential heavy element lines.

3. ABSORPTION LINE CHARACTERIZATION

Figures 2 through 7 show the raw data for our absorption complexes, where we have shifted the various ions to align vertically in redshift/velocity space. When required for clarity we have separated the low-ionization- and high-ionization-potential species for individual systems into different panels.

The zero point of the velocity scales are set to the redshift of the nearest identified galaxy if one is known; when no galaxy is identified we center on the strongest absorption component. The thin solid lines superimposed upon

⁶ When calculating angular size and luminosity distances, we assume a flat cosmology throughout, with $\Omega_M = 0.3, \Omega_\Lambda = 0.7, H_0 = 71$

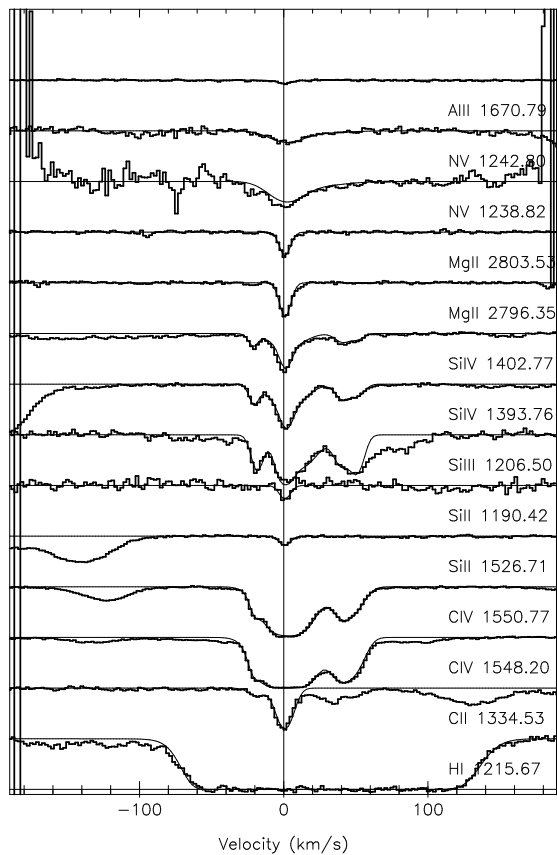


FIG. 2.— Stacked velocity plot of heavy element absorption lines at $z = 1.846$. See Section 4.4.1 for description

the data represent model Voigt profile fits, made using the VPFIT⁷ software package. The output parameters are summarized in Table 2.

3.1. Association of Lines According to Ionization Potential

All six systems exhibit transitions which vary widely in ionization potential, but overlap in velocity space. The most difficult aspect of the fitting procedure was to distinguish which of these ions were physically related, and which were aligned in velocity purely by chance. Intuition provided some guide, in that highly ionized O VI or N V cannot arise in the same gas as nearly neutral species such as Si II, C II, or Fe II. This prior is supported by the velocity profiles: the O VI lines tend to be broad ($b \gtrsim 15$ km/s) and smooth, whereas the low-ionization lines tend to be narrow ($b \lesssim 8$ km/s) and discrete.

The association of C IV and Si IV is less clear. These ions bridge the gap between the high and low potential species, sharing some absorption components with each phase. However, they also contain components not associated with any other ion. In these cases, we looked to our ionization models (described in Section 4) for guidance, iterating between the line fits and models to come upon a physically plausible solution. Our guidelines may be broadly summarized with the following rules:

- O VI and N V components are physically distinct

⁷ <http://www.ast.cam.ac.uk/~rfc/vpfit.html>

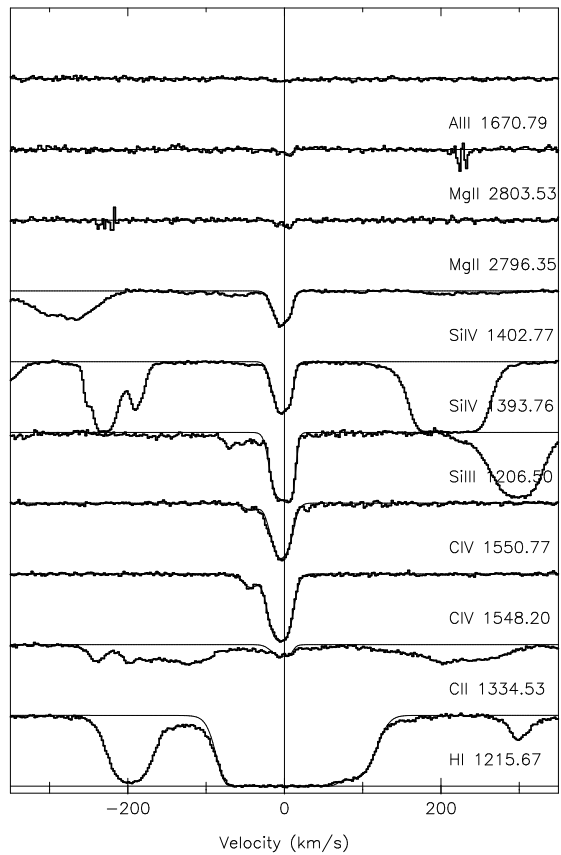


FIG. 3.— Stacked velocity plot of heavy element absorption lines at $z = 2.168$. See Section 4.4.2 for description

from all lines with lower ionization potential than C IV, including Si IV. Although C IV could coexist with O VI, in practice we either do not see C IV at the same redshift as O VI, or the C IV has a different velocity profile and is much too strong to have come from the same gas.

- Fe II cannot come from the same components as Si IV, C IV, or higher ionization potential lines.
- Mg II and Al II can coexist with Si IV or C IV, but only in trace quantities.
- It is possible to observe Si II, Si III, and Si IV, or C II, C III, and C IV simultaneously.

Our tabulated absorption line fits all meet these criteria, but the reader should be aware that they do not represent deterministically unique solutions. We simply established this short set of rules to resolve the degeneracies in our data, with the requirement that the results provide physically realistic inputs for our ionization models.

3.2. Fit Technique, Comments on Robustness

Our procedure has been to fit the singly ionized transitions first (i.e. C II, Si II, Mg II), since these typically have a small number of narrow and easily discernable components. When different ions appeared to originate from the same gas phase (e.g. C II and Si II), we used a feature in VPFIT to “tie” the redshifts of their individual components. This enforces $z_{\text{C II}} = z_{\text{Si II}}$ for the

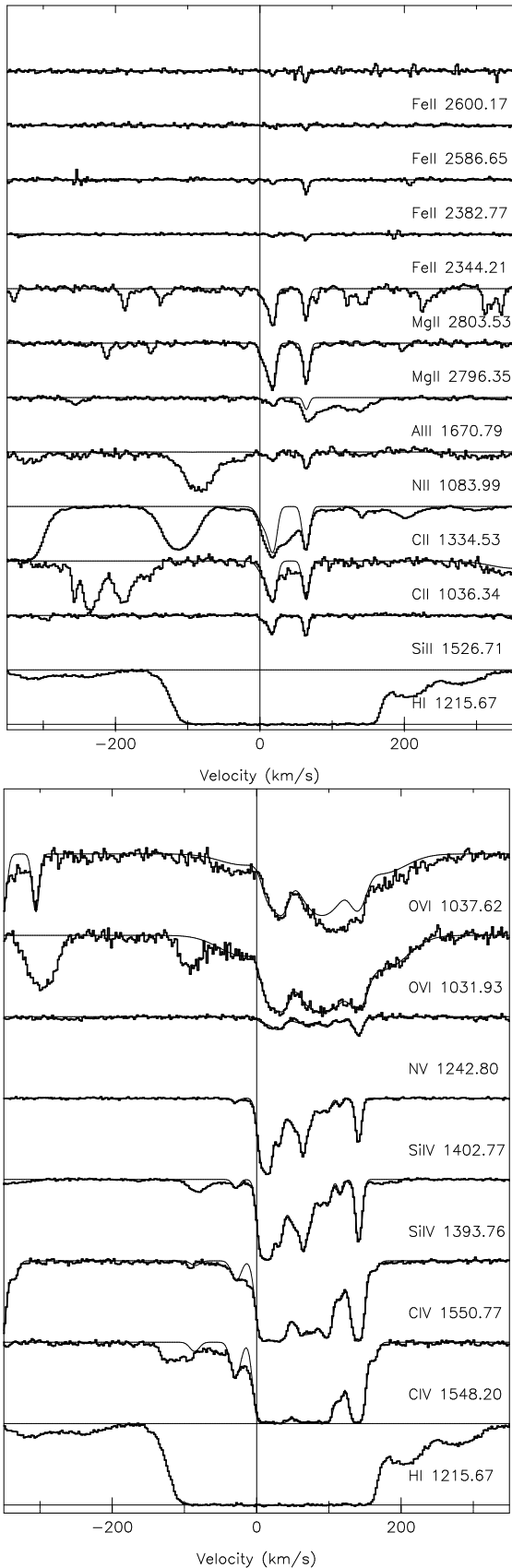


FIG. 4.— Top: Low ionization lines for the system at $z = 2.315$. Zero on the velocity scale corresponds to the redshift of the galaxy Q1700-MD103, which has an impact parameter of $115h_{71}^{-1}$ kpc. Bottom: Highly ionized lines for the same system.

tied components, but allows this redshift to vary during optimization. This is reflected in the tables; when no redshift is listed for a line, it is tied to its predecessor in the list. It is also possible to tie the b parameters of fit components. We used this approach for ions from the same element (e.g. C II, C III, and C IV).

For ions from different elements (with atomic masses m_1 and m_2), the ratio of b parameters can take on values ranging from $b_1/b_2 = \sqrt{m_2/m_1}$ for purely thermal broadening, to $b_1/b_2 \sim 1$, for bulk or turbulent line broadening. By measuring b parameters of elements with different masses, one can in principle solve for the relative contributions of thermal and non-thermal motions to the total line width. This calculation is particularly interesting in our case since both heating and turbulence in the IGM may reveal energy dissipation from nearby starbursts.

Unfortunately, the b parameters are not constrained well enough to permit this type of analysis. Where possible, we did attempt to fit b independently for different elements. However, we encountered two obstacles in interpreting the results. First, the most metal-rich systems had such narrow lines that they were under-resolved or marginally resolved even by HIRES (resolution $\Delta v \approx 6.6$ km/s FWHM, corresponding to $b \approx 4$ km/s). VPFIT accounts for instrumental broadening by convolving a kernel with the model during optimization, so in theory one can estimate linewidths for under-resolved features. However, we have modeled the line-spread function only as a simple Gaussian. This limits our confidence in the measured linewidths for components with $b \lesssim 5$ km/s. However, since these low-ionization lines are very narrow to begin with, they must surely be very quiescent: their temperatures must be very low ($T \lesssim 15,000$ K), and their internal turbulent velocities must be very small ($\Delta v_{\text{turb}} \lesssim 2 - 3$ km/s).

We also found it difficult to estimate b for the higher ionization C IV and Si IV systems because of line blending, and in some cases saturation. As noted previously, the profiles for these ions are very complex, and they seem to trace a range of physical conditions. In the presence of strong blending, the Voigt profile models can take on a range of solutions by trading column densities and b parameters between closely spaced components. Typical uncertainties from these degeneracies amounted to ~ 0.1 dex in column density and $2 - 4$ km/s in b .

The column density measurements for these systems are therefore much more robust than the b parameters. For this reason we have only quoted conservative upper limits on the temperature and turbulent b parameters for most of the systems in Table 2. However, there are a small number of systems where our b estimates are more secure, so we list these values accordingly.

For highly blended systems, the quoted C IV and Si IV column densities are derived assuming thermal relative line widths (indicated in table footnotes). We also fit the same systems with a purely non-thermal ratio of b parameters to gauge the effect on the column densities. The fit quality (χ^2) was similar for the two methods, and the difference in column density was usually smaller than 0.1 dex.

Our most difficult measurements were for H I. The Ly- α transition is heavily saturated for all of the sys-

tems we are considering, yet all are optically thin, as determined by FOS observations of the high-order Lyman continuum (Vogel & Reimers 1995). For several of the higher redshift systems we could observe Ly- β and other H I transitions, and in these examples the high order profiles contained unsaturated regions. However, the lines were usually still blended and/or partially saturated, and at best we could estimate crude upper limits on $N_{\text{H I}}$ from regions where the profiles (whose redshifts and linewidths were inferred from metal lines) leaned up against unsaturated pixels.

Some of H I column densities we report are smaller than the values listed in the Vogel & Reimers (1995) FOS work; this is an important discrepancy since these measurements are crucial for determining absorber metallicities. In the FOS data, $N_{\text{H I}}$ was determined by measuring the discontinuity at the Lyman limit, at much lower resolution ($\Delta v \sim 200 - 270 \text{ km s}^{-1}$ FWHM, compared with our 6.6 km s^{-1}). To compare our measurements with the the FOS data, we use the *total* (i.e. summed) $N_{\text{H I}}$ for all of the high-resolution subcomponents we have fit for each system. For example, in the system at $z = 2.439$ we find a maximum component column density of $\log N_{\text{H I}} = 15.510$, whereas the FOS spectrum yields $\log N_{\text{H I}} = 15.890$. However, at high resolution the system separates into six subcomponents, whose aggregate $\log N_{\text{H I}} = 15.870$ is in excellent agreement with the FOS results.

The match is not always this close, but the median offset for the six measured systems was 0.02 dex, and in five of the six cases our total $N_{\text{H I}}$ limit differed from the FOS value by less than 0.25 dex. The one significant difference was for the system at $z = 2.167$, where our original $N_{\text{H I}}$ was 0.93 dex lower than the FOS measurement. For our HIRES measurement, we had assumed $b = 35 \text{ km s}^{-1}$, appropriate for purely thermal line broadening relative to the heavy element lines. However, Vogel and Reimers' curve-of-growth analysis yielded a somewhat smaller value of $b = 25 \text{ km s}^{-1}$, and we also see some evidence for turbulent line broadening in the relative heavy element linewidths. A choice of 25 km s^{-1} does not conflict with the HIRES profiles, and yields $N_{\text{H I}}$ values similar to the FOS results. Accordingly, we have adopted these values as upper limits on $N_{\text{H I}}$ below. In all other systems we quote the pure best-fit values from the HIRES fits. Although our H I limits are quite rudimentary, they are still internally consistent and provide important constraints on the parameters of our ionization models—particularly the absorber metallicities.

4. IONIZATION MODELING OF THE IGM

We have modeled the physical properties of our absorption line sample using CLOUDY ionization simulations. Since many of the complexes contain absorption from a variety of elements and ionization states, we can gain substantial leverage over the ion balance in individual absorption components.

4.1. Radiation Field

We treated the absorbers as plane-parallel gas slabs, illuminated by the integrated background light from quasars and galaxies. The shape of the background spectrum is derived from an updated calculation based on the work of Haardt & Madau (1996), and provided to us by

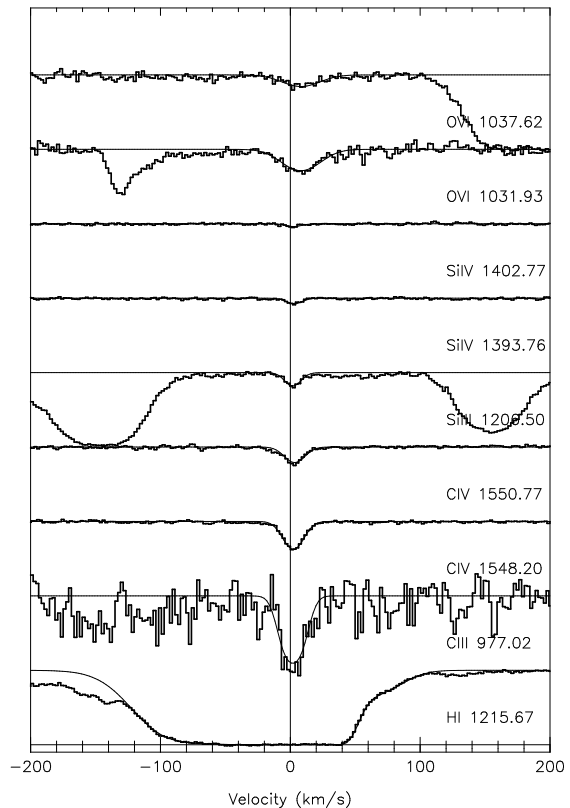


FIG. 5.— Stacked velocity plot of heavy element absorption lines at $z = 2.379$. See Section 4.4.4 for description.

F. Haardt. The new spectrum uses a slightly different power law slope for the shape of intrinsic QSO spectra ($f(\nu) \propto \nu^{-1.8}$), and it also includes an integrated galaxy background. The galaxies contribute primarily at rest-frame optical and near-UV wavelengths, but they also boost the flux blueward of the Lyman limit, where 10% of photons are assumed to escape. We used a separate background spectrum for each absorber in the sample, with a shape and normalization appropriate to its redshift (Scott et al. 2000).

Since the effects of local ionizing sources may be important (Miralda-Escudé 2005; Schaye 2004), we included a crude local radiation model for the two absorption systems which are closest to known high-redshift galaxies. We downloaded synthetic spectra of starburst galaxies from the Starburst99 archive (Leitherer et al. 1999), with properties corresponding to constant star formation models with an age of 300 Myr. We included the effects of in-situ dust extinction by applying the correction of Calzetti et al. (1994), with $E(B - V) = 0.155$. The corresponding escape fraction of Lyman limit photons is $\sim 30\%$, dropping off sharply to the blue. The starburst age and reddening parameters were chosen to match population models of color-selected galaxies at $z \sim 3$ (Shapley et al. 2001). The synthetic spectra were normalized in absolute magnitude to match the observed galaxy apparent magnitudes. Then, the galaxy flux at the location of the absorbing slab was estimated by applying a distance modulus appropriate to the line-of-sight impact parameter for each galaxy (Figure 8). For the nearest system to the sightline, ionizing photons from

the galaxy outnumber those from the metagalactic field by a factor of ≈ 2 ; for all other systems the radiation field at 912\AA was dominated by the diffuse background. One side of the slab was illuminated with this excess local radiation.

4.2. Methodology

Using these background spectra, we generated grids of CLOUDY models whose parameters were varied to reproduce the column densities of each individual absorption line. For every model, we varied the total gas density n_H , which in conjunction with the radiation field determines a system’s ionization balance. We also varied the overall metal content of the gas relative to the solar level, which we denote as $[X/H]$, and the relative $[\text{Si}/\text{C}]$ abundance ratio. The model results are summarized in Table 3. In the following discussion, we use the term “ion” to denote a single absorption line from a single element and ionization state. We refer to a “component” as a set of physically related ions from different elements, whose redshifts match precisely.

Figure 9 demonstrates our methodology. For each component, we defined a set of observed column density ratios to be used as model constraints. Where possible, we favored ratios of ions from the same element (e.g. $\text{C II} / \text{C IV}$, $\text{Si III} / \text{Si IV}$) to eliminate uncertainties arising from the relative abundances between different elements. We compared the selected ratios with their predicted values from CLOUDY to determine the gas density. For a given component, all ion ratios typically matched near a common value of n_H , with only a very weak dependence on metallicity. This best-fit density (determined via simple χ^2) is indicated in the figure with a vertical dashed line.

Next, we combined n_H with CLOUDY-derived ionization fractions to determine the absorbing pathlength for each heavy element ion in the component:

$$L_{\text{ion}} = \frac{N_{\text{ion}}}{n_H \left(\frac{X}{H}\right) f_{\text{ion}}}. \quad (1)$$

Here, N_{ion} represents the ion’s (measured) column density, $(X/H) = (X/H)_{\odot} \times 10^{[X/H]}$ represents the element’s abundance by number relative to hydrogen, and f_{ion} represents the fraction of the element’s atoms in the ionization state of interest. For a fixed radiation field, f_{ion} depends only upon n_H (i.e. n_H determines the “ionization parameter”). After determining L_{ion} for each ion in a component, we averaged the results together to obtain a mean pathlength $\langle L_{\text{ion}} \rangle$ for that component. Only heavy element lines were included in the average since our H I column densities are poorly constrained.

We then inverted Equation 1 to produce model column densities for each ion using the mean pathlength and best-fit model parameters: $N_{\text{model}} = n_H \left(\frac{X}{H}\right) f_{\text{ion}} \langle L_{\text{ion}} \rangle$. The scatter between these model column densities and the observed values is our metric for model accuracy. We minimized χ^2 between the model and data to determine optimal metallicities, while requiring that the implied $N_{\text{H I}}$ satisfied whatever upper limits on $N_{\text{H I}}$ were available.

For some systems, we were able to produce more accurate models by varying the relative $[\text{Si}/\text{C}]$ abundance. This is particularly interesting because $[\text{Si}/\text{C}]$ enhancement is thought to be a signature of enrichment from

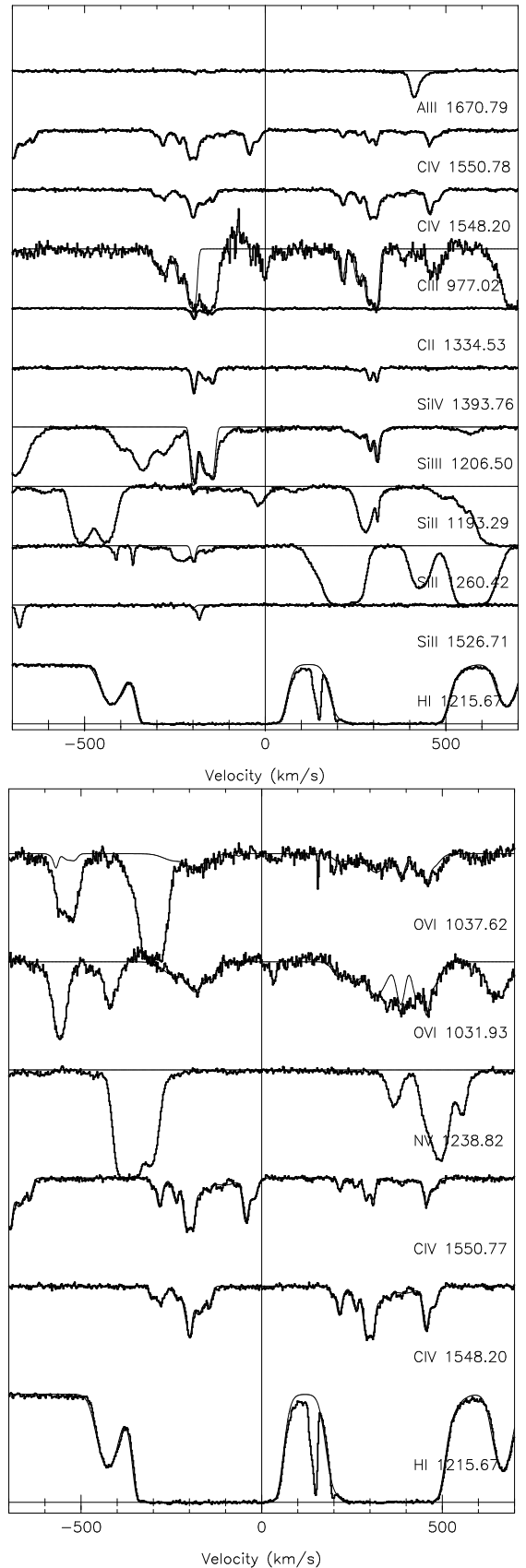


FIG. 6.— Top: Low ionization lines for the system at $z = 2.43$. Zero on the velocity scale corresponds to the redshift of the galaxy Q1700-BX717, which has an impact parameter of 210 kpc. Bottom: Highly ionized lines for the same system.

Type II supernovae. We approached this measurement cautiously, since a $[\text{Si}/\text{C}]$ enhancement can be degenerate with a change in gas density (ionization parameter) and we did not want to stretch our model past what is warranted from the available data. For this reason, we only tested $[\text{Si}/\text{C}]$ variations for components where we could break this degeneracy by constraining the ionization parameter *independently* using ratios from the same element, as in $\text{Si II} / \text{Si IV}$, $\text{Si III} / \text{Si IV}$, or $\text{C II} / \text{C IV}$. With the density and hence ionization balances determined, we examined a single ratio— $\text{Si IV} / \text{C IV}$ —to estimate $[\text{Si}/\text{C}]$.

4.3. CLOUDY Results

Table 3 summarizes the results from our ionization models. For each component, the best-fit values for the three model variables—metallicity, density, and (if applicable) $[\text{Si}/\text{C}]$ —are listed first. Then we show several cloud parameters that follow from the optimal model, including (L_{ion}) , $N_{\text{H I}}$, and the equilibrium gas temperature T_{eq} . In the rightmost column we list the suite of ions used to constrain each component’s ionization model.

We have also quoted crude confidence intervals on the model parameters for each component. It is not straightforward to estimate conventional errors for these model parameters, since ambiguities in the Voigt profile fitting or model assumptions can compound in ways that are not necessarily obvious. However, we tested a wide range of model parameters for each component⁸, and the data clearly excluded significant portions of this search space in each case. The sub/superscript numbers in the table span the full range of values permitted by the data. They are not standard deviations propagated in traditional fashion, but they do provide a feel for the model uncertainties.

4.4. Descriptions of Individual Galaxy/Absorber Systems

In this section we provide a brief interpretation of the model output for each system in the absorption sample, together with a description of nearby galaxies. We quote redshift differences in velocity units, which may be mapped to distances using the Hubble parameter, which at $z = 2.3$ takes a value of $H = 240h_{71}^{-1} \text{ km s}^{-1} \text{ Mpc}^{-1}$, not accounting for peculiar velocities.

A key question concerns how far in impact parameter and/or velocity separation we can allow galaxies and absorbers to be separated while still considering them to be physically associated. Theoretical models of supernova-driven winds at $z \lesssim 5$ tend to find stalling radii near ~ 100 kpc, with the limit set by a combination of energetics and travel time (Aguirre et al. 2001b; Fujita et al. 2004; Bruscoli et al. 2003; Kollmeier et al. 2005; Benson et al. 2003). Especially given the large mass estimates for the galaxies in our sample ($M_{\text{halo}} \sim 10^{11-12} M_{\odot}$, Adelberger et al. 2005b), it may be difficult to eject much interstellar mass to larger distances. However, outflowing material is seen directly in high redshift galaxy spectra, blueshifted by $\Delta v \sim 350 \pm 250 \text{ km s}^{-1}$ relative to the stellar rest frame. While it is possible

⁸ The full range of parameters we examined was $-3 \leq [\text{X}/\text{H}] \leq 0.5$, $-5.5 \leq n_{\text{H}} \leq -1.0$, and $-1 \leq [\text{Si}/\text{C}] \leq 1$.

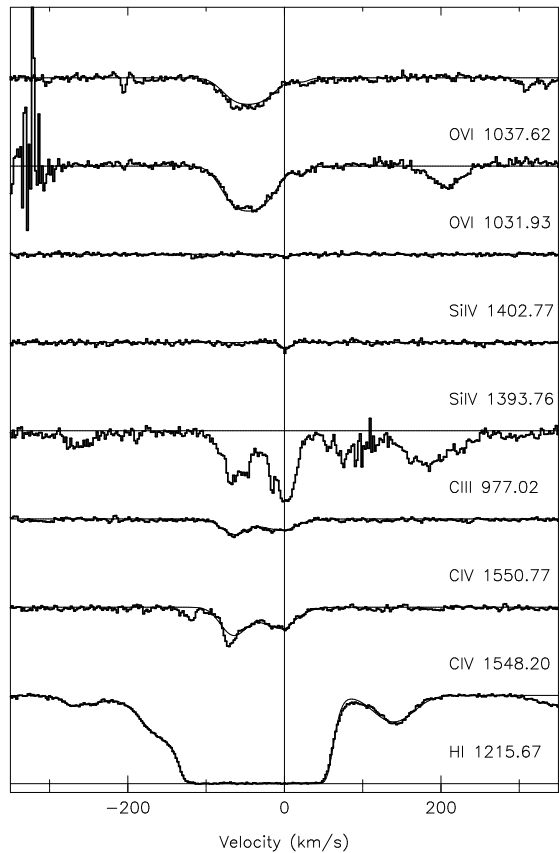


FIG. 7.— Stacked velocity plot of heavy element absorption lines at $z = 2.578$. See Section 4.4.6 for description.

that the winds contain hot gas moving at higher speeds (up to $\sim 1000 \text{ km s}^{-1}$), the material with the largest geometric cross-section for QSO absorption should also be moving tangential to the QSO sightline, so its projected line-of-sight velocity should be systematically smaller at larger impact parameters. In the following discussion, we consider strong galaxy/absorber associations to be systems where the galaxy and absorber are separated by $\lesssim 200$ kpc in impact parameter and/or $\Delta v \lesssim 600 \text{ km s}^{-1}$ in velocity. A more detailed justification of these choices will be presented further below in Section 6.3.

4.4.1. $z = 1.846$ (Figure 2)

This complex was identified via N V , but it also contains a number of other, lower ionization potential lines. We do not identify any galaxies with this absorber; the closest candidate (BX635), is still quite far at $327h_{71}^{-1}$ proper kpc from the quasar sightline and 1500 km/s in redshift space. The C II , Si II , and Mg II absorption is narrow and unresolved—this system is very cold and kinematically quiescent. It was difficult to measure $N_{\text{H I}}$ since our spectrum only covered $\text{Ly-}\alpha$. We estimated upper limits by fixing H I components at the redshifts of the metal lines, setting their b parameters to the values appropriate for thermal broadening, and increasing $N_{\text{H I}}$ to match the wings of the absorption. The resulting $N_{\text{H I}}$ matched the FOS measurements of Vogel & Reimers (1995) to within 0.1 dex. The FOS spectrum shows some evidence of O VI absorption, though the doublet appears to suffer from blending at

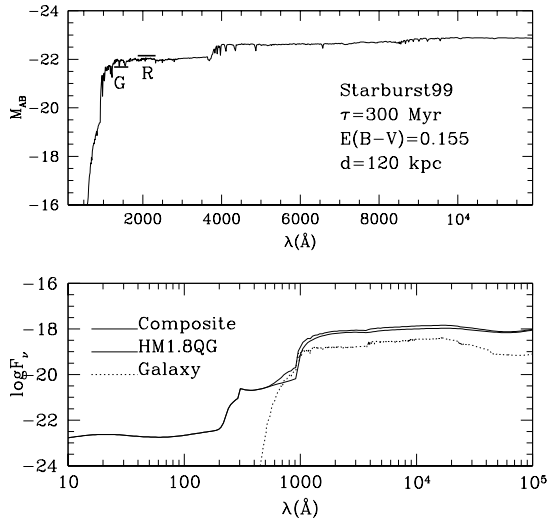


FIG. 8.— Starburst background for MD103 ($z = 2.315$). To account for the effects of local radiation, we added the spectrum of a starburst galaxy to the standard Haardt & Madau spectrum for the extragalactic background field. The template spectrum was a 300Myr-old galaxy taken from the Starburst99 archive, adjusted for dust reddening according to a Calzetti et al. (1994) law with $E(B - V) = 0.155$. This age and reddening were chosen to match observations of $z \sim 3$ Lyman break galaxies. The spectrum was scaled to reproduce the observed G and R band luminosities (Top panel), and then projected to a distance corresponding to the galaxy’s impact parameter from the QSO sightline. The bottom panel shows the individual spectra of the galaxy (at the location of the absorber), and the Haardt & Madau background, and finally the combined spectrum, which was used for all ionization models of this system. Most of the UV photons from the galaxy are extinguished by dust, though there may be some local flux contribution near the Lyman limit.

the observed resolution. Our best-fit CLOUDY models find a near-solar metallicity, with a minimum plausible value of $\sim \frac{1}{3}Z_{\odot}$. The gas density is near $10^{-2.5} \text{ cm}^{-3}$, or $\rho/\bar{\rho} \sim 300$ times the cosmic mean, and the absorbing pathlengths are of order $\Delta L \sim 100$ pc. The dense environment and high abundances suggest that this system was enriched very recently by an unidentified galaxy that is either fainter than $R = 25.5$, or whose colors fell outside of the UGR selection space (See Section 2.1).

4.4.2. $z = 2.168$ (Figure 3)

This system was identified based on the detection of several carbon and silicon transitions, along with Mg II and Al II . It is ambiguous whether this system contains O VI , since the entire O VI region is saturated by interloping $\text{Ly-}\beta$ lines. However, there is clearly no N V . There is also no obvious galaxy association; the nearest candidate is BX691 which has an impact parameter of $\rho = 290h_{71}^{-1}$ kpc but $\Delta v = +2000$ km/s from the absorber. Our initial fits to the HIRES data (assuming thermal broadening of H I relative to the metal lines) found $N_{\text{H I}} \lesssim 10^{15.9}$ for $b = 35 \text{ km s}^{-1}$. For these values the CLOUDY model finds a metallicity of $\sim \frac{1}{10}$ solar or higher, with $\Delta L \sim 100$ pc and $\rho/\bar{\rho} \sim 300$.

However, as described in Section 3.2, measurements of the Lyman limit discontinuity using FOS imply $N_{\text{H I}} \sim 10^{16.8}$ and $b = 25 \text{ km s}^{-1}$. The carbon and silicon linewidths in the HIRES spectrum show evidence of tur-

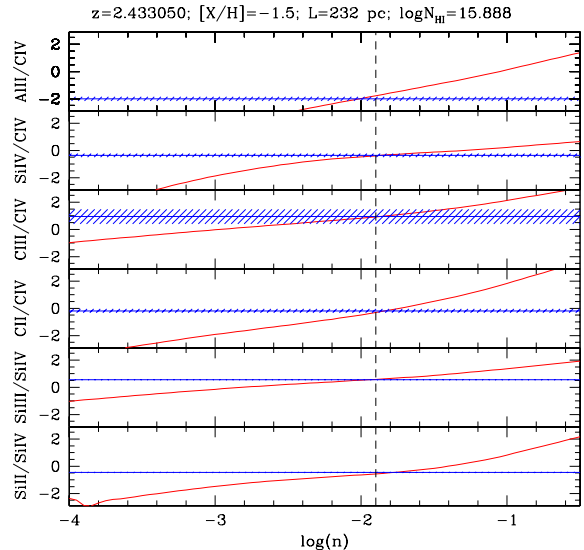


FIG. 9.— Sample ionization model for a component in the complex at $z \sim 2.43$. Measured ion ratios with 1σ errors are shown by blue horizontal lines with hatched regions. CLOUDY predictions are shown with red solid lines. Vertical dashed line indicates the density which yields the best match between the data and model. This system has $[X/H] = -1.5$ ($\sim \frac{1}{30}Z_{\odot}$), $n_{\text{H}} = 10^{-1.9} \text{ cm}^{-3}$ ($\rho/\bar{\rho} \sim 1000$), $\Delta L = 232$ pc, and $[\text{Si}/\text{C}] = +0.37$

bulent line broadening at the $b_{\text{turb}} \sim 10 - 15 \text{ km s}^{-1}$ level; this would be sufficient to bring the total $\text{H I } b$ parameter and column density into a range consistent with FOS. Adoption of the higher $N_{\text{H I}}$ value changes the model metallicities substantially, allowing values as low as $[X/H] \sim -2.5$, at sizes of 1 kpc and larger, and densities of $\rho/\bar{\rho} \sim 100 - 1000$. Given the sensitivity of $N_{\text{H I}}$ to the assumed b parameter, the metallicity for this system is fairly uncertain. However, it does appear to be quite over-dense. It may be mildly enriched by a galaxy that remains unidentified, or it may represent a particularly dense and stirred-up gas cloud with a metallicity comparable to the surrounding IGM.

4.4.3. $z = 2.315$ (Figure 4)

This is the strongest system in the absorption sample, and it is located at the same redshift as the closest galaxy to the QSO sightline. MD103 is one of the more luminous galaxies near HS1700. Stellar population models incorporating rest-frame IR photometry from Spitzer/IRAC find a stellar mass of $M_{*} \sim 10^{11} M_{\odot}$, and a (somewhat uncertain) star formation age of $t_{\text{sf}} \sim 300 - 1000$ Myr (Shapley et al. 2005). The stellar mass ranks MD103 among the top $\sim 10 - 15\%$ of galaxies at $z \sim 2.3$. It also has a large $\text{H}\alpha$ equivalent width, implying a substantial star formation rate—in the range of $64 - 88 M_{\odot} \text{ yr}^{-1}$ (dust corrected, Erb et al. 2003).

Strong O VI absorption reveals hot gas in the IGM surrounding MD103. We also detect N V , though it appears to be kinematically associated with C IV rather than O VI . Mixed in with this material are small regions of very cool, very dense, very metal-rich material. These components are narrow and unresolved, but they contain absorption from Fe II , which is only seen in

extremely dense environments. Their ionization models yield solar metallicity, $\rho/\bar{\rho} \sim 10,000$, and sizes of ~ 1 pc. There are also many components seen in C IV and Si IV, which seem to trace gas with intermediate temperatures and densities. This combination of shock-heating, vigorous cooling, high densities, solar metal enrichment, and a star-forming galaxy, all suggest that the HS1700 sight-line is piercing a feedback mixing zone where debris from MD103 is being deposited into the IGM at $R \sim 100$ kpc.

4.4.4. $z = 2.379$ (Figure 5)

This is the simplest system in our absorption line sample. None of the observed galaxies can plausibly be linked with the IGM absorption. Our best-fit CLOUDY model predicts a metallicity of $\sim \frac{1}{100}$ solar, densities near $\rho/\bar{\rho} \sim 100$, and sizes of several kpc for the component traced by carbon and silicon. There is also a clear O VI detection with no corresponding N V. The highly ionized component is slightly offset in redshift, and can be explained equally well by a hot, collisionally ionized plasma, or a low density ($\rho/\bar{\rho} \lesssim 10$), large ($\Delta L \sim 10 - 100$ kpc) photoionized structure. This complex probably represents a clump of material embedded in a modestly enriched intergalactic filament. Its metallicity is only $\sim 1\sigma$ above the cosmic median, and there is little else to suggest vigorous feedback in the immediate neighborhood.

4.4.5. $z = 2.43$ (Figure 6)

This absorption system is coincident in redshift with the galaxy BX717. Like MD103, BX717's luminosity is at or slightly below average for $z \sim 2.5$ galaxies, but it is forming stars at a rate of $\sim 20M_{\odot} \text{ yr}^{-1}$ (Erb et al. 2003). Population models yield an integrated stellar mass of $M_{*} \sim 10^{10}M_{\odot}$ for BX717, with a stellar age of 400 – 500 Myr (Shapley et al. 2005). The QSO absorption system has a distinctive double-trothed profile, with the strongest components situated approximately $\Delta v = -200$ km/s and +350 km/s from BX717. It is tempting to interpret this as a signature of expanding walls of a wind bubble originating from the galaxy. However, given BX717's somewhat large impact parameter ($\rho = 216h_{71}^{-1}$ physical kpc) it is at least as likely that the double trothed shape is merely coincidental.

The CLOUDY models yield intermediate metallicities near $\sim \frac{1}{30}$ solar—about a factor of 10 higher than the IGM. The gas densities are in the $\rho/\bar{\rho} \sim 1000 - 3000$ range, with absorbing pathlengths of several hundred parsecs to a kiloparsec. We detect broad, but somewhat weak O VI absorption with no corresponding N V, which we interpret as hot gas with $T \sim 300,000$ K. It is difficult to say whether the heavy elements originated in BX717, or in an unidentified companion galaxy.

4.4.6. $z = 2.578$ (Figure 7)

This simple system has an unusually broad and featureless C IV profile, and a strong O VI line. The best fit model yields a pathlength of several kpc, with overdensity $\rho/\bar{\rho} \sim 50 - 100$ and clear [Si/C] enhancement. The O VI absorption is most likely produced in hot gas, though a low density, photoionized solution is possible if the structure is extremely large ($L \gtrsim 100$ kpc). The nearest galaxy (MD119), is offset in redshift by

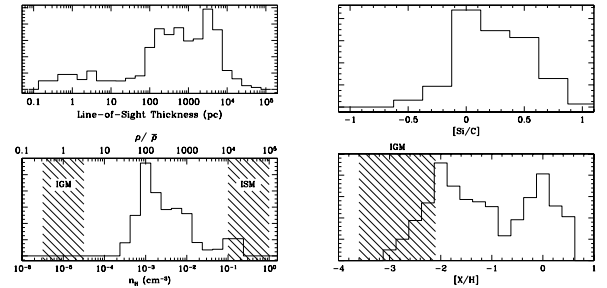


FIG. 10.— Parameter histograms for our CLOUDY models of absorption components. These are not simple histograms of the best-fit values; rather, for each component we account for the contribution throughout the uncertainty interval quoted in Table 3, assuming that the probability distribution is flat within this range. Our sample selects absorbers with small thicknesses ($L \sim 1$ kpc), high densities ($\rho/\bar{\rho} \gtrsim 100$), and [Si/C] abundance enhancements. The metallicities are distributed well above the intergalactic median, and show evidence of bimodality.

$\Delta v \sim 1000$ km/s and has a fairly large impact parameter ($\rho = 336h_{71}^{-1}$ physical kpc). MD119 is probably not responsible for the QSO absorption, though it may be embedded in a related larger structure. In fact this system resembles an unusually metal-rich filament or group environment more than a shock-heated wind.

4.5. Overview of Model Results and Comments on Robustness

Figure 10 summarizes the distribution of model parameters for our full absorption line sample. We have constructed these histograms using a slightly unusual method. Rather than assigning each component to a single bin, we spread its contribution over the full range of bins encompassed by its errors, normalizing so that its total addition to all bins equals one unit. Thus, a component with large model uncertainties adds a small amount to many bins, while a well-constrained system may add a single count to a single bin. The final distributions approximate probability densities for the parameters, marginalized from our multi-dimensional search space.

The most noticeable result in Figure 10 is a tendency toward small cloud sizes and high metallicities. For the majority of our systems the best-fit metallicity ranges from $0.01 - 1 Z_{\odot}$, with some evidence for bimodality in the distribution. For comparison, the general IGM has a median abundance of $\sim \frac{1}{700}Z_{\odot}$; its $\pm 1\sigma$ abundance contours for $z \sim 2.5$ are shaded in the figure (Simcoe et al. 2004; Schaye et al. 2003). It appears that these absorption systems are chemically polluted relative to the universe at large. Systems in the upper half of the bimodal distribution have abundances of at least $\frac{1}{3}Z_{\odot}$. This makes them even more metal rich than the interstellar gas contained within many high redshift galaxies (Pettini et al. 2001, 2002; Shapley et al. 2004). They are most likely the product of recent galaxy formation and feedback. The lower half of the metallicity distribution may trace slightly older galactic debris which has been diluted upon mixing into the IGM, or even true intergalactic gas which was pre-enriched by much earlier episodes of star formation.

Line-of-sight absorber thicknesses of a few hundred

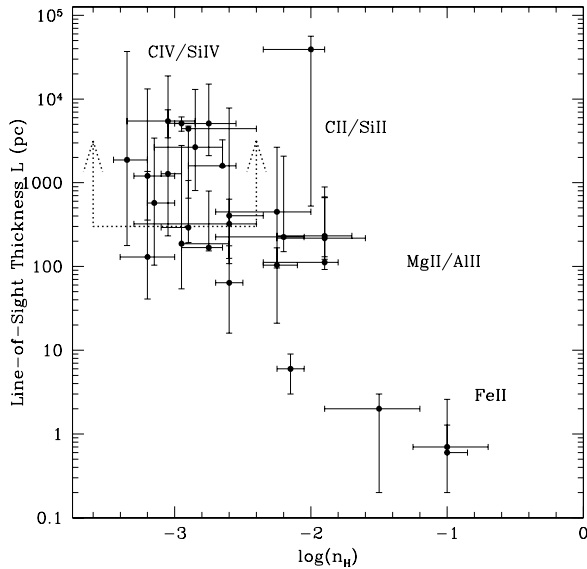


FIG. 11.— Correlation between absorber density and “size” (line-of-sight absorbing pathlength). There is a rough sequence of absorption line properties following from upper left to lower right in the diagram. The largest, lowest density absorbers are highly ionized and seen exclusively in C IV and/or Si IV. Moving downward, one observes species with increasingly lower ionization potential, initially picking up C II and Si II, then Mg II and Al II, and finally Fe II in the smallest, densest pockets. Dotted arrows indicate the smallest approximate transverse sizes of C IV absorbers, estimated from double-sightline observations of lensed quasars (Rauch et al. 2001).

parsecs to a few kpc are typical, though some of the most metal-rich systems are even sub-parsec in scale. These sizes are consistent with the *transverse* scales of C IV systems derived from multi-sightline analysis of lensed QSOs (Rauch et al. 2001). The absorbing structures must therefore be quite small, or contain substantial substructure if they are organized into larger units. The best-fit gas densities are several orders of magnitude higher than the mean density of the IGM at $z \sim 2.5$, but somewhat lower than the characteristic density of galactic interstellar media.

In the systems where we could measure $[\text{Si}/\text{C}]$, there is some evidence for a relative silicon abundance enhancement by 0.1-0.5 dex. This is roughly consistent with heavy element yield calculations for Type II supernovae, which predict a similar $[\text{Si}/\text{C}]$ boost (Woosley & Weaver 1995; Umeda & Nomoto 2002; Chieffi & Limongi 2004), so it is possible that the metal-rich absorbers are preferentially enriched by debris from the explosion of high-mass stars.

Though we have displayed the model results as histograms, in practice the parameters can be correlated. For example, in Figure 11 we show a scatter plot of n_H versus ΔL which illustrates how the properties of the metal-rich absorbers fall along a rough sequence. At the top of this sequence are the C IV and Si IV components, which have sizes of one to several kpc and low densities. Moving to higher densities one encounters smaller structures traced by lower ionization potential lines, from C II /Si II, to Mg II /Al II, and finally Fe II at extremely small sizes and high densities. This sequence is a useful

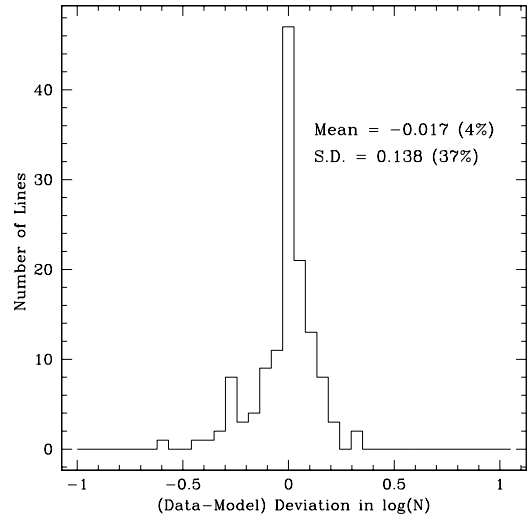


FIG. 12.— Histogram of the difference between $\log(N_{\text{meas}})$ —the Voigt profile column density for each ion in the sample—and the best-fit model predictions from CLOUDY. The models on average reproduce the data with no statistically significant systematic offset. Expressed in linear terms, the typical scatter for an individual line is $\sim 37\%$.

tool for estimating the physical conditions in a given absorption system at a glance, based on what low-ionization lines are visible. The absence of points in the lower left corner of the plot is a selection effect; we would not be sensitive to very small, low density systems. However, systems in the upper right quadrant should be detectable if they are present. A larger sample containing Lyman limit and damped Ly- α systems might populate this corner of the plot. Their absence in this small sample illustrates that the optically thin, metal-rich absorbers are more common than their optically thick counterparts, and hence must have a larger statistical cross-section.

Among the model parameters we have measured, the gas density n_H is most robust, since it is determined solely from ratios of heavy element ions and mostly insensitive to variations in metallicity in the optically thin limit. The uncertainty in metallicity was larger, since its primary constraint comes from difficult H I measurements. For a small number of systems the heavy element ratios changed just enough with metallicity to rule out very low values. However, we usually used the upper limit on $N_{\text{H I}}$, measured from unsaturated regions of the Ly- β or higher order profiles, to determine a lower bound on $[\text{X}/\text{H}]$. Even with such weak H I constraints, the corresponding lower limits on $[\text{X}/\text{H}]$ are often still significant.

A measure of the models’ accuracy is the overall scatter between their predicted ion column densities and the true observations. A histogram of this metric is shown in Figure 12, and the individual model column densities are listed at the far right of Table 2 for comparison with the true measurements. We see no statistically significant systematic offset between our model column densities and the data, but there is a residual RMS scatter of ~ 0.14 dex. This reflects the combined error from the Voigt profile fits, the model assumptions, and from within CLOUDY itself. Put another way, our models reproduce the observed column densities with a *linear*

accuracy of $\sim 37\%$ or better.

5. PHYSICAL PROPERTIES OF THE METAL-RICH ABSORPTION-LINE SYSTEMS

So far we have shown that our absorption sample—identified primarily by strong O VI, but supplemented with one N V and one Mg II system—identifies compact, dense clouds with unusually high heavy element abundances. In the next two sections we consider a simple explanation for these properties, involving the propagation of bubble-like shocks through intergalactic filaments. The absorbers’ high abundances strongly suggest that the shocks are being expelled from—rather than falling into—star forming regions.

5.1. Arguments for a Sheet- or Shell-Like Absorber Geometry

To see even a handful of metal-rich absorption systems in a single sightline, the aggregate cross-section of the population must be significant. We estimate their average cross-section in the standard fashion:

$$N = n\sigma \frac{c}{H_0} \Delta X \quad (2)$$

where N is the number of detections in the quasar spectrum, n is the comoving number density of the absorbing structures, and ΔX is the absorption pathlength probed along the sightline⁹. Assuming a circular cross section, $N = 3$,¹⁰ $\Delta X = 2.9$ for our HS1700 spectrum, and comoving number density n , we calculate the cross-sectional physical radius as:

$$R \sim 190 h_{71}^{-1} \text{ kpc} \left(\frac{n}{0.0021 \text{ Mpc}^{-3}} \right)^{-\frac{1}{2}}. \quad (\text{Shell geometry}) \quad (3)$$

Here we have normalized the comoving number density to that of $R \leq 25.5$, UV-selected, $z \sim 2.3$ galaxies as determined by Adelberger et al. (2005b). Clearly this cloud radius R is much larger than the inferred absorber thickness $\Delta L \sim 1$ kpc (see Figure 10). Apparently if one associates the metal-rich absorbers with luminous galaxies, their geometry must resemble a thin sheet or shell.

Alternatively, if the absorption arises from a random distribution of much smaller, spherically symmetric clouds with $\sigma \sim \pi(\Delta L/2)^2$, the implied comoving density is extremely large:

$$\frac{n_{\text{abs}}}{n_{\text{gal}}} \sim 150,000 \left(\frac{\Delta L}{1 \text{ kpc}} \right)^{-2} \quad (\text{Cloudlet geometry}) \quad (4)$$

i.e., the absorbers outnumber known $z \sim 2.3$ galaxies by over 5 orders of magnitude. The enhancement can be

⁹ The pathlength is given by

$\Delta X = (1+z) [\Omega_M(1+z) + \Omega_\Lambda/(1+z)^2]^{-\frac{1}{2}} \Delta z$ for $\Omega = 1$. We searched the range $1.8 \leq z \leq 2.7$ for a total $\Delta x = 2.9$. The search boundaries were determined by signal-to-noise ratio considerations in the blue, and a desire to avoid the proximity effect near the QSO in the red.

¹⁰ For the following analysis we exclude the systems at $z = 2.379$ and $z = 2.568$, since they have lower heavy element abundances and gas densities than the most metal-rich systems in the sample. We also exclude the system at $z = 2.168$; its gas density is high, but its metallicity is poorly constrained and could be substantially below solar levels.

severe, since the smallest systems in our sample have $\Delta L \sim 1$ pc but are seen in many of the metal-rich complexes. For comparison, the Local Group contains ~ 20 – 25 known low mass objects per L^* galaxy. Another perspective comes from simple Press-Schechter (1974) considerations (e.g, Mo & White 2002): if observable galaxies at $z \sim 2.3$ have total masses of $M \sim 10^{12} M_\odot$ (Adelberger et al. 2005b), then the mass of the dark matter haloes that outnumber these galaxies by a factor of $\sim 10^5$ is $\lesssim 10^6 M_\odot$ —smaller than globular clusters.

These statistics are reminiscent of the “weak” Mg II absorbers seen locally (Churchill et al. 1999; Rigby et al. 2002), and the arguments for their sizes, metallicities, and number densities are essentially identical. In fact several of our systems would qualify as weak Mg II systems; the complex at $z = 2.315$ in particular resembles the “iron-rich” class of weak Mg II absorbers, which have ~ 1 pc scale absorption depths and near-solar metallicities. However, in the high redshift data there is evidence of a connection between these cool, dense systems and strong O VI absorption. This is an important clue that the metal-rich systems were recently shock-heated and have subsequently cooled into their present state.

Small dense cloudlets like these would not be in pressure equilibrium with the IGM. Their characteristic gas density of $\log(n_H) \gtrsim -3$ represents an enhancement of $\rho/\bar{\rho} \gtrsim 100$ relative to the cosmic mean at $z \sim 2.3$, even as their optically thin interiors are maintained at a similar temperature as the exterior IGM through photoionization ($T \sim 5,000 - 15,000$ K for clouds versus $T \sim 20,000 - 30,000$ K for the IGM). The cloudlet pressure therefore exceeds that of the IGM by a factor of $\sim 10 - 100$. This will cause them to puff into the IGM on a timescale comparable to their sound crossing time, which for a system with $R \sim 500$ pc and $c_s \sim 16$ km s⁻¹ is roughly 30 Myr. Even if the clouds are embedded in $10^6 M_\odot$ dark matter haloes, the gravitational potential is too weak to confine the gas, since the sound speed (~ 16 km s⁻¹) exceeds the halo escape velocity ($\sim 5 - 10$ km s⁻¹) even well within the halo. It would be very difficult to self-enrich such a halo to solar levels, since it is doubtful that the baryons would survive even a single supernova event.

These arguments favor the sheet or bubble scenario over one involving a large population of small cloudlets. The shells have high chemical abundances and are mixed with hot O VI gas, suggesting shock heating and a recent association with star-forming environments. In other words, the metals at large galactocentric radii probably originated in the interstellar medium of nearby galaxies and were ejected violently into the IGM. The presence of luminous galaxies within $\sim 250 h_{71}^{-1}$ kpc of half the absorbers bolsters this hypothesis.

Any realistic model of these sheets or bubbles would probably not be symmetric or monolithic, since the shocks propagate through a non-uniform medium and may develop hydrodynamic instabilities. Clumping of material within the sheets would lead to somewhat larger radii in Equation 3. However, this only reinforces the basic result: sheets or bubbles provide the most efficient geometry to create a large absorption cross-section from structures with small linear dimensions.

5.2. Radiative Shocks as a Likely Origin for Metal-Rich Absorbers

A natural location to form thin shells or sheets is at the interface of shock fronts, particularly when the shocks have become radiatively efficient. Order-of-magnitude calculations show that a metal rich, radiative shock propagating through the IGM will generate conditions much like those observed in the metal-rich absorbers.

During the early evolution of a strong shock when radiative losses are insignificant, $\approx 75\%$ of the shock's kinetic energy is used in heating the post-shock material, so $T = \frac{3}{16} \frac{\mu m_H}{k} v_{\text{shock}}^2$, which with m_H as the proton mass and $\mu = 0.62$ (for fully ionized gas) yields:

$$T \approx 10^6 \text{ K} \left(\frac{v_{\text{shock}}}{265 \text{ km s}^{-1}} \right)^2. \quad (5)$$

At $T \gtrsim 10^6 \text{ K}$, the cooling timescale for post-shock gas can be quite long. However, in time the shock will decelerate (e.g. from ram pressure, or from gravity and pdV work in the case of galactic winds) and the post-shock temperature will descend into the peak region of the cooling curve, near 300,000 K. This transition occurs at $v_{\text{shock}} \sim 145 \text{ km s}^{-1}$. At this point, the shock becomes radiatively efficient, and a thin dense shell is formed which travels at the bulk speed of the shock front. In a radiative (isothermal) shock, the pre- and post-shock temperatures are identical since the shock's thermal energy is radiated away on timescales that are short compared to the system's evolutionary timescale.

In this situation, the post-shock gas density relates to the pre-shock value as $n_{\text{post}} \approx \mathcal{M}^2 n_{\text{pre}}$, where $\mathcal{M} = v_{\text{shock}}/c_s$ is the Mach number, i.e. the shock front velocity in units of the sound speed in the undisturbed medium. By continuity across the shock boundary, we also have $v_{\text{post}} \approx v_{\text{pre}}/\mathcal{M}^2$. In the $z \sim 2.5$ IGM, the sound speed is roughly $c_s \sim \sqrt{kT/\mu m_H} \sim 16 \text{ km s}^{-1} T_{20}^{0.5}$, where T_{20} is the temperature of the general IGM normalized to 20,000 K (Schaye et al. 2000). Since the shock becomes radiative at $v \sim 145 \text{ km/s}$, the Mach number at the time of this transition is $\mathcal{M} \sim 9 T_{20}^{-0.5}$, which yields the following values for the density and post-shock velocities:

$$n_{\text{shell}} \sim 10^{-2.1} \text{ cm}^{-3} \times \left(\frac{n_{\text{IGM}}}{10^{-4} \text{ cm}^{-3}} \right) \left(\frac{T_{\text{IGM}}}{20,000 \text{ K}} \right)^{-1} \left(\frac{\mathcal{M}}{9} \right)^2 \quad (6)$$

$$v_{\text{post}} \sim 1.8 \text{ km s}^{-1} \left(\frac{T_{\text{IGM}}}{20,000 \text{ K}} \right) \left(\frac{\mathcal{M}}{9} \right)^{-2}. \quad (7)$$

Here we have assumed that the shock is travelling through an intergalactic filament with $\rho/\bar{\rho} = 10$ relative to the cosmic mean density $\bar{n} \approx 10^{-5}$ (for $z \sim 2.5$). Note that v_{post} is not the speed of the shock, but rather the speed of post-shock gas in the frame of the shock, which is still moving at over 100 km s^{-1} . The number density n_{shock} for filaments with $\rho/\bar{\rho} \sim 1 - 10$ may be compared with the observed distribution of n_H shown in Figure 10. For consistency we can also verify that the cooling timescale of the shocked, ionized gas is short:

$$\tau_{\text{cool}} \sim \frac{3n_{\text{shell}}kT}{n_{\text{shell}}^2\Lambda} \quad (8)$$

$$\sim 0.5 \text{ Myr} \left(\frac{n_{\text{IGM}}}{10^{-4} \text{ cm}^{-3}} \right)^{-1} \left(\frac{T_{\text{IGM}}}{20,000 \text{ K}} \right)^{-1} \times \left(\frac{v_{\text{shock}}}{145 \text{ km s}^{-1}} \right)^2 \left(\frac{\Lambda(T)}{10^{-21} \text{ erg cm}^3 \text{ s}^{-1}} \right)^{-1} \quad (9)$$

where $\Lambda(T)$ is the gas cooling function from Sutherland & Dopita (1993) evaluated at 300,000 K (or the temperature given by Equation 5). This rapid thermalization with the background radiation field lends *ex post facto* support to the CLOUDY models developed in Section 4 under the assumption of photoionization equilibrium.

A crude estimate of the shell thickness is given by the product of the shock's propagation timescale and post-shock gas velocity. If the shocks are produced during galaxy assembly, and have timescales similar to the star formation ages of $z \sim 2.5$ galaxies (Shapley et al. 2005), we find:

$$\Delta L \sim v_{\text{post}} \tau_{\text{sf}} \quad (10)$$

$$\sim 550 \text{ pc} \left(\frac{T_{\text{IGM}}}{20,000 \text{ K}} \right) \left(\frac{\tau_{\text{sf}}}{300 \text{ Myr}} \right) \left(\frac{\mathcal{M}}{9} \right)^{-2} \quad (11)$$

This distance is also comparable to the line-of-sight absorber thicknesses shown in Figure 10. Evidently, the large compressions achieved in radiative shocks give rise to compact, high-density shells with densities and thicknesses similar to the observed values.

Finally, using the above calculations we may estimate the H I column density of the radiative shock front:

$$N_{\text{H I}} \sim n_{\text{shell}} \cdot \Delta L \cdot f_{\text{H I}} \quad (12)$$

$$\sim 10^{16.5} \text{ cm}^{-2} \left(\frac{\tau_{\text{sf}}}{300 \text{ Myr}} \right) \left(\frac{n_{\text{IGM}}}{10^{-4} \text{ cm}^{-3}} \right) \left(\frac{f_{\text{H I}}}{10^{-2.5}} \right) \quad (13)$$

Here we have made use of our CLOUDY grid to determine the proper value of $f_{\text{H I}}$ for the post-shock density given in Equation 6, and solar heavy element abundances. This column density is generally consistent with our observations, though it is on the high end of the distribution. This discrepancy is easily reconciled if the gas metallicity is reduced even to $Z/Z_{\odot} \sim 0.1$ (thereby lowering $f_{\text{H I}}$), or if the ambient filament overdensity is reduced below $\rho/\bar{\rho} \lesssim 10$. The important point is that these systems have much higher column densities than typical Ly- α forest lines, but they are still optically thin in H I.

The strong shocks present at earlier times should produce hot material that has a long cooling time. The O VI absorption in our sample may be a residue from this earlier stage. In principle one could also catch a young system before its shock begins to radiate, in which case it would be visible in O VI but not in H I or lower ionization lines. We did not detect this type of system in a survey of several quasar sightlines (Simcoe et al. 2002), but they may exist in smaller numbers. The relative rarity of O VI-only QSO absorbers is naturally explained by galactic wind models since the shell's cross section grows as it cools. This is particularly true if the radiatively-inefficient shock phase is short lived.

The mere presence of O VI absorption does not require one to interpret a particular absorption system as a feedback candidate. In fact we do not report O VI detections

for two systems in our sample, though its presence is not ruled out in either case (one exhibits N v but has a redshift too low for ground-based O VI measurements, while the other is blanketed by interloping Ly- β absorption). One can alternatively produce O VI via accretion shock heating as in the low redshift IGM (Davé et al. 2001), or through pure photoionization of low density gas (e.g. Chaffee et al. 1986). In fact, we have argued that some of the systems in our sample arise from some of these very mechanisms. However, the combination of (1) strong but optically thin H I, (2) strong absorption from both high and low ionization potential carbon, silicon, magnesium, and iron, (3) highly ionized gas, and (4) an association with galaxies together provides a strong case for the feedback interpretation in several of the systems in our sample.

6. DISCUSSION

We have presented data and ionization models for six strong absorption systems in the HS1700+6416 sightline. Five of these were selected based upon the detection of highly ionized gas (O VI and/or N v); the sixth was identified by its weak Mg II absorption. Half of these systems are very metal-rich, with abundances ranging from $\frac{1}{30}$ solar to solar levels. Each of the metal-rich absorbers contains small ($\lesssim 100$ pc) pockets of very dense, enriched material. We have also shown that these systems' number statistics and absorption properties are consistent with an origin in thin, radiatively efficient shocks. This, together with their high abundances, suggests that these systems represent debris from galaxy formation, where material ejected from the proto-galaxy's interstellar medium is mixing into the nearby IGM.

6.1. *The Galaxy Environment of High-Metallicity Absorbers*

Luminous galaxies are located near over half of the metal-rich systems (2 of 3), at essentially identical redshift and small impact parameter ($\rho \lesssim 200h_{71}^{-1}$ kpc). These galaxy-absorber systems are also reported by Adelberger et al. (2005a), based upon the same dataset. The strongest system ($z = 2.315$, MD103) appears to be associated with the closest galaxy to the quasar sightline, though it is still more than 100 kpc distant. If the metal-rich systems result from winds or merger feedback, then roughly equal numbers of feedback zones (weighted by cross-section) at $z \sim 2.5 - 3.5$ may have come from luminous Lyman-break-type objects, and unidentified galaxies which are either fainter than $R = 25.5$ or have different colors than known $z \sim 2.5$ galaxy populations.

Several investigators have uncovered evidence for correlations between luminous galaxies and C IV absorbers both in the local universe (Chen et al. 2001) and afar (Adelberger et al. 2003, 2005a). This absorption has variously been ascribed either to accretion of pre-enriched intergalactic gas (Haehnelt et al. 1996; Rauch et al. 1997a) or dwarf satellites (Chen et al. 2001) during hierarchical galaxy assembly, or to the expulsion of metal-rich material from star-forming galaxies (Adelberger et al. 2003, 2005a).

It is somewhat unlikely that the present absorption sample is produced by accretion alone; the observed metal abundances ($Z/Z_{\odot} \sim 0.1 - 1$) are higher than one

would expect in such a scenario ($Z/Z_{\odot} \sim 10^{-2.8}$). Simulations of gas infall tend to reproduce the properties of general C IV systems (Haehnelt et al. 1996; Rauch et al. 1997a), but they do not always follow the high-end tail of the metallicity distribution traced by our sample. We argue below that infall of material that is pre-enriched at high redshift ($z \gtrsim 5$) may explain the majority of C IV systems in the “field,” but that the strongest metal line systems—particularly those containing O VI—are probably related to more recent galaxy formation.

If this interpretation is correct, then some of the enriched gas is probably expelled from galaxies slightly below the magnitude limits of present high redshift surveys (recall that half of the absorbers do *not* have an associated galaxy). While even bright nearby galaxies could remain unidentified due to color effects, there are reasons relating to wind energetics that a fainter population might be favored. Since less massive galaxies are more numerous, the absorption cross section becomes smaller according to Equation 3; at the same time the smaller mass results in lower halo escape velocities. Dark matter haloes in the range $M_{\text{DM}} \sim 10^{10} - 10^{11} M_{\odot}$ should outnumber known $z \sim 2.3$ galaxies by about an order of magnitude (Mo & White 2002), which would reduce the bubble radius to $R \sim 70$ kpc—a distance well within reach for theoretical models of supernova-driven galactic winds (Aguirre et al. 2001b).

Alternatively, to enrich the IGM to near-solar levels through purely dynamical processes, one would need to shred the ISM of a forming galaxy during the merger/assembly process, but after several generations of stars have had time to enrich the gas. The characteristic velocities (several hundred km s^{-1} , Barkana 2004) and timescales (several hundred Myr) should be similar for superwinds and slingshot mergers. However, the merger would need to be arranged so as to distribute its debris fairly uniformly, rather than in one-dimensional tails which have small absorption cross-sections. One possible solution to this problem involves the adiabatic expansion of winds whose thermal energy is provided by shock-heating from mergers, rather than supernovae (Cox et al. 2004).

The lower metallicity systems in our absorption sample have lower gas densities and larger sizes ($\Delta L \gtrsim 5$ kpc line-of-sight). These systems resemble moderately enriched large-scale structures, and have metallicities within 1σ of the mean level observed in the Ly- α forest. Their O VI absorption may arise in accretion shocks associated with collapsing structures or they may trace quite large ($L \sim 100$ kpc) photoionized structures—our models cannot distinguish between these two possibilities. No galaxy candidates have been identified for these systems.

6.2. *A Galaxy Cluster Near an O VI System*

There is evidence that one reported galaxy-absorber pair lies at the outskirts of a proto-cluster at $z \sim 2.310$ (Steidel et al. 2005). This raises the possibility that the shock-heated O VI gas represents intra-cluster matter rather than halo gas from the nearest individual galaxy. The few galaxy clusters known at $z \gtrsim 2$ do not resemble the virialized, relaxed structures seen in the local universe, though they may subsequently evolve into such a state (Steidel et al. 1998; Pentericci et al. 2000;

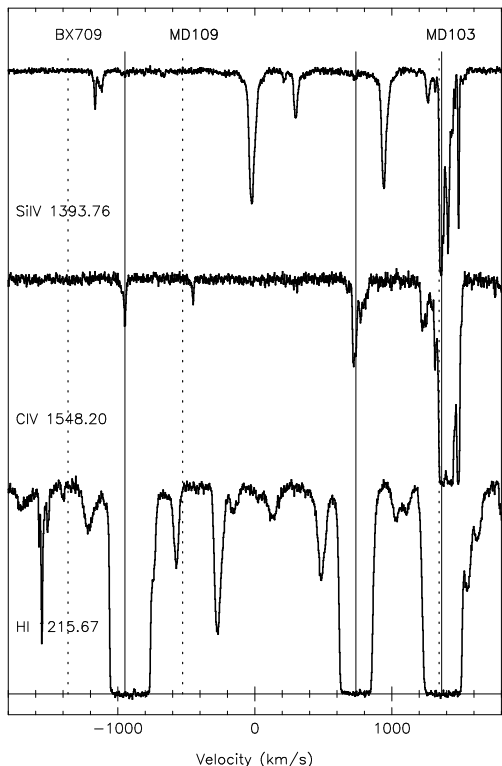


FIG. 13.— H I, C IV, and Si IV portions of HS1700 absorption line spectrum, centered on the redshift of galaxy proto-cluster reported by (Steidel et al. 2005). The velocity range shown approximately matches the redshift extent of the galaxy overdensity. We detect three metal absorption line systems in the cluster neighborhood, indicated with solid vertical lines. Redshifts of galaxies within $\rho \leq 500h_{71}^{-1}$ physical kpc of the QSO sightline are indicated with vertical dashed lines and labeled accordingly. The systems at -100 and +800 km/s are typical of “field” C IV absorbers in terms of C IV /H I and Si IV /C IV ratios. They do not have galaxies that correspond closely in redshift, although the system at -1000 km/s is flanked by two galaxies that may be embedded in a common large-scale structure. The system at +1400 km/s is clearly much more metal-rich, and is characteristic of the sample of radiative shock systems explored in this paper. We do not detect diffuse O VI or N V that would indicate shock-heated intra-cluster gas.

Kurk et al. 2000; Venemans et al. 2002). The high redshift clusters exhibit clear galaxy overdensities, but they are somewhat large both on the sky ($L \gtrsim 10$ Mpc) and in redshift space ($\Delta z \sim 0.05$, $\Delta v \gtrsim 3000$ km s $^{-1}$).

In Figure 13 we plot the absorption profiles of several ions throughout the entire galaxy overdensity ($2.285 \leq z < 2.315$; $\Delta v \sim 3000$ km s $^{-1}$). We detect three significant Ly- α absorbers with C IV at $\Delta v \sim -900$, +750, and +1400 km s $^{-1}$ relative to galaxy overdensity’s center at $z = 2.300$. The detection of several significant Ly- α absorbers is consistent with the results of Adelberger et al. (2003), who also find large Ly- α opacities near proto-clusters at $z \sim 3$. However, it is clear that the system at $\Delta v \sim +1400$ km s $^{-1}$ is qualitatively different from the other two Ly- α absorbers; in fact this is the MD103 galaxy/absorber complex described in Section 4.4.3, underscoring the distinctive nature of the O VI -selected metal line systems.

The other two systems are also strong H I absorbers with $N_{\text{H I}} \sim 10^{16}$, but they have much lower Si IV /C IV ratios indicating a higher degree of ionization,

and lower C IV /H I which indicates a lower heavy element abundance ($[X/H] \lesssim -2.0$). They are not accompanied by hot O VI or N V. The system at $\Delta v \sim -1000$ km s $^{-1}$ (relative to the cluster center) is flanked both on the sky and in redshift space by a pair of galaxies (MD109 and BX709) with impact parameters of $\rho = 208$ and 316 kpc and $\Delta v = \pm 400$ km s $^{-1}$ (relative to the absorber). Their orientation on the sky is indicated in Figure 1. This configuration could easily result from the galaxies being embedded in a large filament whose gas has been pre-enriched at earlier times to a level near the intergalactic mean.

There are several weak H I lines with $N_{\text{H I}} \sim 10^{12}$ cm $^{-2}$ dispersed throughout the galaxy overdensity, but we do not detect any diffuse O VI or N V gas that would indicate the presence of a shocked intra-cluster medium (ICM). There are no absorbers at the central redshift of the galaxy overdensity. On the whole, the data do not show evidence of uniform, highly enriched gas in the proto-cluster environment at $z \sim 2.3$. However, roughly solar abundances are observed near the closest galaxy to the line of sight. This suggests that the metals and shock heating are powered by dynamical processes associated with the galaxy itself rather than interactions with the cluster. If MD103 and other galaxies in the congealing proto-cluster are losing their interstellar media through winds or dynamical interactions, this could produce substantial intra-cluster enrichment even before the ICM appears to have virialized.

6.3. The Absorption Environment of Color-Selected Galaxies

Having described the galaxy population in absorption-selected environments, we now consider the inverse problem: characterization of the IGM near a sample of color-selected galaxies. Figure 14 shows a montage of absorption line plots centered on the redshifts of nine galaxies from Table 1. The plots are sorted according to galaxy-absorber impact parameter, from upper left to lower right. For each panel we show the profiles of H I, C IV, and Si IV.

There appears to be a qualitative change in the properties of the IGM at galaxy-absorber impact parameters $\rho \sim 320h_{71}^{-1}$ kpc. Inside this radius, all five detected galaxies have strongly saturated Ly- α absorption at $\Delta v \lesssim 500$ km s $^{-1}$; four of the five are also C IV systems. At impact parameters larger than $\sim 320h_{71}^{-1}$ kpc, we see no trends in the absorption data that would suggest an association with galaxies. The only absorption near BX635 is Ly- β from a higher redshift system (which we have masked in the figure). The raw C IV and Si IV profiles from BX635 are contaminated by interloping Ly- α ; we verified that these lines could not be masking true C IV or Si IV, since at least one of the doublet components was free of Ly- α across the profiles. For presentation purposes, we fit the profiles of the interloping Ly- α near BX635 and removed their signatures. MD119 exhibits fairly unremarkable Ly- α forest lines, and BX759 and MD92 have very weak H I profiles. Except for MD119 the systems at $\rho \geq 320h_{71}^{-1}$ kpc exhibit no heavy element absorption.

Figure 15 shows a graphical representation of these trends. In the bottom panel, we plot the column density of the strongest H I line located within $\Delta v = 500$ km/s of

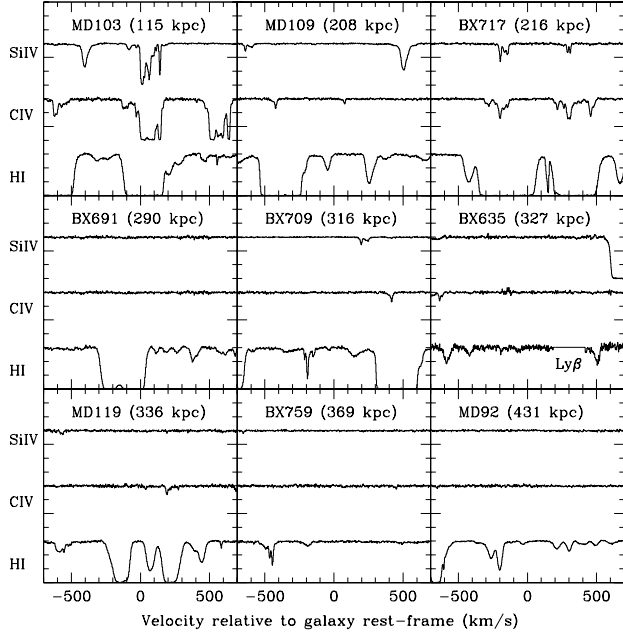


FIG. 14.— Montage of H I, C IV, and Si IV absorption in the vicinity of the $z \sim 2.5$ galaxies listed in Table 1. The systems are arranged from top left to bottom right in order of increasing impact parameter. Beyond $\sim 320h_{71}^{-1}$ kpc, the absorption properties resemble typical Ly- α forest regions with no distinct metal absorption. We have removed interloping Ly- α lines from the the C IV and Si IV profiles of BX635 (see text).

each galaxy redshift, as a function of galaxy/absorber impact parameter. There is an apparent dropoff in H I column at $\rho \sim 300h_{71}^{-1}$ kpc, with smaller impact parameters exhibiting $N_{\text{H I}} \sim 10^{15.5-16}$ and larger ones showing $N_{\text{H I}} \sim 10^{12.5-13.5}$. Using the formulae of Schaye (2001) one can translate these H I column densities into approximate baryonic overdensities; this scaling is shown at the right of the bottom panel. Galaxies close to the sightline tend to reside in regions with $\rho/\bar{\rho} \sim 30 - 100$, whereas separations of $\gtrsim 300h_{71}^{-1}$ kpc tend to yield densities near or slightly below the cosmic mean.

The simplest interpretation is that the galaxies are embedded in gas-rich intergalactic structures with transverse scales on the sky of ~ 300 physical kpc (~ 1 comoving Mpc), similar to the scales reported by (Adelberger et al. 2005a). The structures are revealed through moderately strong Ly- α forest absorption with either no heavy element lines (e.g., BX691), or abundances consistent with the cosmic mean (e.g., BX709, MD109). In other words, luminous galaxies reside in regions resembling randomly chosen, moderately overdense filaments, as one would expect from hierarchical structure formation models.

The top panel of Figure 15 shows the variation of heavy element abundance in the IGM with galaxy impact parameter. The metallicity estimates were made in the manner described in Section 4, using multiple ion measurements coupled with CLOUDY models. The data’s sensitivity did not permit abundance measurements in the low density IGM (i.e. beyond $300h_{71}^{-1}$ kpc), nor could we measure abundances lower than $[X/H] \sim -3$. How-

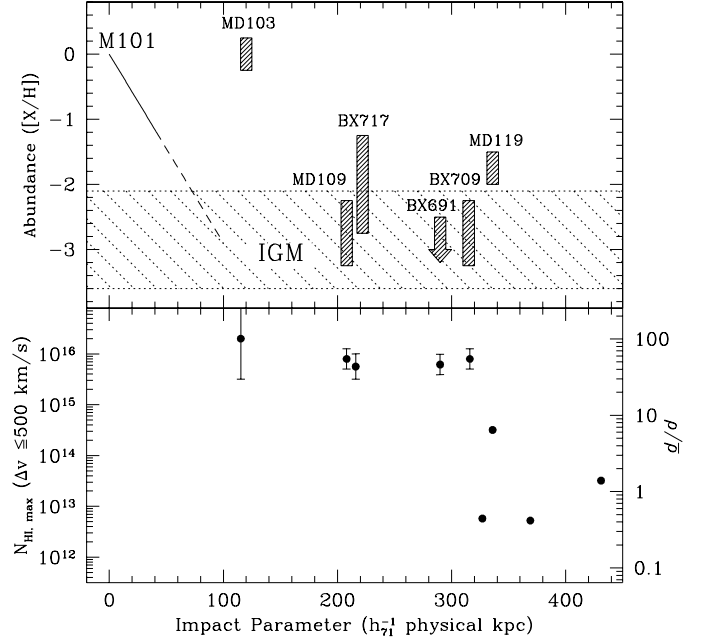


FIG. 15.— Variation of gas density (bottom) and chemical abundance (top) in the IGM as a function of galaxy impact parameter. The gas density shows evidence of a marked decline at impact parameters of $\sim 300h_{71}^{-1}$ kpc, which we interpret as the transverse scale of gas structures where the galaxies are embedded. Errors in $N_{\text{H I}}$ for points at large radii are smaller than symbols. The chemical abundances are very high at small impact parameter, but blend into the background field (shown with hatched bar) between $100 - 200h_{71}^{-1}$ kpc. The large intergalactic metallicity near MD103 cannot be explained by extrapolation of in-situ disk enrichment trends—for reference, we show the abundance gradient of the local galaxy M101’s H II regions as a function of galactocentric radius (Kennicutt et al. 2003). Solid line represents measurement area, while the dotted line is an extrapolation of the measured trend.

ever, the systems that we measured show some interesting trends that might not be expected from hierarchical structure formation alone.

In the $200 \lesssim \rho \lesssim 320h_{71}^{-1}$ kpc range which is most heavily populated by our sample, the chemical abundances are comparable to general Ly- α forest systems, whose mean $\pm 1\sigma$ contours are shown in the plot with a horizontal hatched bar (Simcoe et al. 2004; Schaye et al. 2003). Though individual systems appear to scatter above the mean, we remind the reader that we cannot measure the low-metallicity end of the distribution (e.g., we only measure an upper limit for BX691).

The one galaxy in our sample with $\rho \lesssim 200h_{71}^{-1}$ kpc (MD103) exhibits a marked enhancement in metallicity above the general IGM. This ~ 300 -fold abundance jump is not consistent with a simple extrapolation of in-situ galactic disk enrichment trends. For comparison we show the radial abundance gradient of M101, one of the best-studied disk galaxies in the local universe (Kennicutt et al. 2003). The extrapolated metallicity merges into the general IGM at radii of ~ 80 kpc; high redshift Damped Ly- α systems generally follow this relation as well (Chen et al. 2005). BX717 also shows evidence of enhanced metallicity, though at larger impact parameter the effect is not as strong.

This suggests that local metal enrichment does affect the chemistry of the IGM in the immediate surroundings of high redshift galaxies, and that the metal-rich debris can travel distances of $100 \lesssim \rho \lesssim 200h_{71}^{-1}$ kpc before being substantially diluted by intergalactic matter. This encompasses an appreciable portion of the gas structures where the galaxies reside ($\rho \lesssim 300h_{71}^{-1}$ kpc), but not the entire volume. However, in cosmological simulations, overdense filamentary structures only occupy $\sim 1 - 5\%$ of the total volume (Miralda-Escude et al. 1996), so the cosmic filling factor of the outflowing material is still probably quite small unless it escapes preferentially into voids where it could remain undetected (see also Section 6.5).

The ejection of interstellar heavy elements could be accomplished via supernova-driven winds associated with star formation, or it could be the result of tidal interactions and ram pressure stripping during the galaxy assembly process. Observationally it will be difficult to distinguish between these two scenarios (or both effects working in concert), since all are manifested by shock-heated, metal rich regions in the vicinity of massive galaxies. There is independent support for the superwind hypothesis from the outflows observed in galaxy spectra (Franx et al. 1997; Pettini et al. 2001), but the energy budget required to drive winds from massive galaxies is quite large (Mac Low & Ferrara 1999). Alternatively, since the observed $z \sim 2.3$ galaxies have characteristic total masses of $\sim 10^{12}M_{\odot}$ (Adelberger et al. 2005b) they must have undergone several major mergers if the hierarchical galaxy formation paradigm is correct. Gnedin (1998) has argued that dynamical interactions associated with the merger process can account for most of the intergalactic metal enrichment, but other simulations show exactly the opposite result—that tidal disruption contributes negligibly to intergalactic abundances, and supernova ejecta dominate (Aguirre et al. 2001b).

Even if recent, local metal enrichment is important at $\rho \sim 100$ kpc, it is not clear that the heavy elements at $\rho \sim 200 - 300h_{71}^{-1}$ kpc were deposited by these same late-time processes. Theoretical arguments based on supernova energetics (Fujita et al. 2004; Bruscoli et al. 2003; Kollmeier et al. 2005; Benson et al. 2003) and travel times (Aguirre et al. 2001a,b) all stress the difficulty of blowing superwinds at $z \lesssim 5$ much farther than 100 kpc. Particularly for large galaxies with $M \sim 10^{11-12}M_{\odot}$, it appears difficult for supernovae alone to propel substantial portions of ISM past the escape velocity, though it may be easier to preferentially remove metal-rich material (Mac Low & Ferrara 1999). In addition, ultra-powerful winds could create large-scale hydrodynamic disturbances in the Ly- α forest, in contradiction with observations of a quiescent intergalactic velocity field (Rauch et al. 2005).

Nevertheless, outflows are seen directly in high redshift galaxy spectra—even for systems with $M_{\text{halo}} \sim 10^{11-12}$ (Steidel et al. 2004; Adelberger et al. 2005b; Pettini et al. 2001; Franx et al. 1997). The ejecta travel at $v \sim 250$ km s $^{-1}$, and their deep absorption troughs imply large covering factors, such that the wind material is at least $\geq 1 - 2$ half-light radii from the galaxy center. If these velocities and radii represent the true initial conditions, then most calculations find terminal shell radii of ~ 100 kpc (Aguirre et al. 2001b; Furlanetto & Loeb

2003), with the limit determined by gravity, ram pressure, and travel time. On the other hand, the observable wind material could trace matter at larger radii whose velocity has already been attenuated from a faster starting speed. Or, the visible low-ionization lines may only trace one phase of the total wind, which is dominated by hot gas moving at $v \gtrsim 1000$ km s $^{-1}$.

In the absence of better constrained initial wind parameters, it will remain difficult to determine beyond reasonable doubt whether the metals at $\rho \gtrsim 200h_{71}^{-1}$ kpc originated in late-time winds (Adelberger et al. 2003), or whether they were already present in the IGM from earlier times (e.g., Madau et al. 2001). Our observations support the claim that absorption within $\rho = 100 - 200h_{71}^{-1}$ kpc of galaxies provides a snapshot of ongoing galaxy feedback. Indeed, MD103 is a clear example of a massive ($\sim 10^{12}M_{\odot}$) galaxy affecting the IGM as far away as $R \sim 100$ kpc. If the outflows reach even larger radii, it may pose a challenge for theoretical wind models, as well as measurements of Ly- α forest turbulence and estimates of early metal enrichment in the IGM (Pettini et al. 2003; Songaila 2001).

6.4. The Chemical Dilution of Feedback Debris

Consider a shell with mass M_{ej} and initial metallicity Z_{ej} that is ejected into the IGM via supernovae or a dynamical disruption. Over time the shell will sweep up metal-poor ambient matter, diluting its chemical content. The average metallicity of the shell may be expressed as:

$$\langle Z \rangle = \frac{Z_{\text{ej}}M_{\text{ej}} + Z_{\text{IGM}}M_{\text{swept}}}{M_{\text{ej}} + M_{\text{swept}}} \quad (14)$$

$$\approx Z_{\text{ej}} \left(1 + \frac{M_{\text{swept}}}{M_{\text{ej}}} \right)^{-1}. \quad (15)$$

The approximation in Equation 15 refers to early times when $Z_{\text{ej}} \gg Z_{\text{IGM}}$ and $M_{\text{ej}} \gg M_{\text{swept}}$. It underscores how chemical dilution is only significant when the wind's swept-up mass exceeds the mass of the initial ejecta.

For a given redshift, the expansion radius where this transition occurs depends on the choice of M_{ej} , which is not well constrained on either theoretical or observational grounds. One guess motivated by observations of local starbursts is $M_{\text{ej}} \approx M_{*}$, since these systems' mass outflow rates are comparable to their star formation rates (Martin 1999). However, high abundances have been measured in the interstellar media of high redshift galaxies (Shapley et al. 2004), so a substantial fraction of their metals must have been retained over time. If we assume mass loss fractions of $[0.01, 0.1]M_{*}$, a fiducial galaxy stellar mass of $M_{*} \sim 2 \times 10^{10}M_{\odot}$ (Shapley et al. 2005), and an ambient density of $\rho/\bar{\rho} = 10$, we find that the debris must travel $R \sim [55, 120]$ kpc before its metallicity is reduced by 1 dex.

Thus if interstellar material can escape dynamically from massive galaxies at $z \sim 2.5 - 4$, it could plausibly travel more than $R \gtrsim 100$ kpc before blending into the background metallicity field. Once the total shell mass becomes dominated by entrained material, its metallicity will decrease as R_{shell}^{-3} , or roughly 1 dex for every factor of 2 in radius. Accordingly the metals would begin to blend into the surrounding IGM at $R \sim 100 - 200$ kpc, much like what is shown in Figure 15. The scatter

about this simple scaling may be very large for individual galaxies, since the particular conditions (galaxy mass, merger history, supernova rate, mass loss, ejection velocity) vary widely from system to system. However, with a statistical sample over many sightlines one could test this generic mixing prescription and in principle measure the heavy element yield of early galaxies.

6.5. Galaxy Formation Feedback in a Cosmological Context

If the metal-rich absorbers indeed penetrate feedback mixing zones, it is natural to ask what portion of the IGM is affected by the process. Absorption line samples are often useful for addressing such problems since they are cross-section selected and therefore relatively unbiased with respect to luminosity. For a galactic wind the system cross-section is time-dependent, and represents a complicated interplay between the starburst energetics, the progenitor’s halo mass, and the shell’s entrainment and mixing with surrounding matter.

In this context, we remind the reader that these absorbers represent a small fraction of all Ly- α forest lines, or even C IV systems in general. A cursory examination of the total C IV region in our HS1700 spectrum yielded 16 C IV detections, so the metal-rich systems probably encompass only $\sim \frac{1}{4} - \frac{1}{3}$ of all C IV absorbers (depending upon whether one counts the systems at $z = 2.37$ and $z = 2.568$ as “metal-rich”). The remaining 60-70% of C IV systems have lower C IV /H I ratios typical of the tenuous IGM, where $[C/H] \sim -2.8$ (Simcoe et al. 2004; Schaye et al. 2003; Songaila & Cowie 1996). Likewise, over the same redshift range there should be ~ 160 detectable H I lines with $N_{\text{H I}} \geq 10^{12.5}$ (Kim et al. 2001).

One can phrase this point another way by calculating the mass fraction of the Ly- α forest that is encompassed by our sample of metal-rich feedback systems. Since we have already calculated ionization corrected gas densities and sizes for the absorbers, we can use the values from Table 3 to estimate the mass density of feedback zones:

$$\Omega_{\text{feedback}} = \left(\frac{1}{\rho_c} \right) \cdot \mu m_H \cdot \frac{\sum n_H \Delta L}{\frac{c}{H_0} \sum \Delta X}. \quad (16)$$

Summing over all components from the metal-rich absorption systems ($z = 1.846, 2.315,$ and 2.43) and excluding collisionally ionized O VI components, we find $\Omega_{\text{feedback}} = 0.00061$. We can account statistically for the additional mass at $T \sim 10^{5-6}$ K using O VI measurements from Simcoe et al. (2002), who find $\Omega_{\text{O VI}} \sim 0.00032(Z/0.5Z_{\odot})^{-1}(f_{\text{O VI}}/0.2)^{-1}$, i.e. a contribution comparable to the cooler feedback material. The Ly- α forest encompasses $\sim 90\%$ of all baryons at $z \sim 2.3$ (Rauch et al. 1997b; Weinberg et al. 1997), so for an assumed $\Omega_b h^2 = 0.024$ (Spergel et al. 2003; O’Meara et al. 2001) and equal amounts of O VI and cooler feedback material we find:

$$\frac{\Omega_{\text{feedback}}}{\Omega_{\text{forest}}} \sim 3\%. \quad (17)$$

Evidently the shock-heated, high-metallicity regions (i.e. the systems most clearly related to feedback) only represent a small fraction of the total mass in the Ly- α forest, unless their mass is dominated by a very hot phase with $T \gtrsim 10^{6-7}$ K. Gas at these temperatures is seen in

X-ray observations of low redshift starbursts, though it would be nearly impossible to detect at $z \sim 2.3$. Also, if the cooler, lower metallicity C IV systems at larger radii are tepid remnants of powerful winds at $z \sim 2 - 4$ the mass fraction of feedback systems could increase by a factor of a few. Even then the majority of baryons are still found at densities near the cosmic mean, where individual C IV systems cannot be measured for cross-correlation with galaxies.

While the metal-rich systems comprise a small fraction of all Ly- α and C IV systems by *number*, they may represent a significant amount of the total C IV *mass* in the universe. This can be seen by examining the customary formula for calculating the contribution of C IV to closure density (Lanzetta 1993):

$$\Omega_{\text{C IV}} = \frac{H_0 m_{\text{C IV}}}{c \rho_{\text{crit}}} \int_{N_{\text{min}}}^{N_{\text{max}}} N f(N) dN \quad (18)$$

where $f(N)$ represents the number of C IV systems per unit column density per unit absorption pathlength, and N_{min} and N_{max} represent the minimum and maximum C IV mass in the absorption line sample. Songaila (2001) finds a power-law form for $f(N)$ with slope $f(N) \propto N^{-1.8}$ at $z = 2.90 - 3.54$, which implies that $\Omega_{\text{C IV}} \propto (N_{\text{max}}^{0.2} - N_{\text{min}}^{0.2})$. Accordingly, C IV mass density calculations are always dominated by the few highest column density systems in a sample, which are heavily represented among the metal-rich systems studied here. In fact, the systems chosen for our modeling analysis are the six strongest C IV absorbers of the 16 total toward HS1700 (recall that they were not selected according to $N_{\text{C IV}}$); all have at least one component with $N_{\text{C IV}} > 10^{13}$. Of the remaining 10 C IV systems, only one has $N_{\text{C IV}} = 10^{13.007}$; all the rest have $N_{\text{C IV}} \leq 10^{13}$.

This is an important consideration for studies of early metal enrichment in the IGM via measurements of $\Omega_{\text{C IV}}$ (Pettini et al. 2003; Songaila 2001). Since high-redshift ($z \gtrsim 5$) QSO observations are often undertaken at lower spectral resolution and/or signal-to-noise ratios, the line samples used for these measurements may be disproportionately populated with strong C IV systems. If these trace dense, metal-rich structures like the ones presented here, the $\Omega_{\text{C IV}}$ measurements may not in fact be tracing chemical enrichment in tenuous regions of the IGM. Instead, the ionization and chemistry may be governed more locally, e.g. by galaxies and feedback (as suggested in Pettini et al. 2003, Section 6). This provides a possible explanation of the observed lack of evolution in $\Omega_{\text{C IV}}$ with redshift: at each epoch the strongest C IV lines may provide an instantaneous snapshot of regions which are actively undergoing chemical enrichment and being illuminated by local stars, rather than an integral of global enrichment in the background-illuminated “field” C IV systems over cosmic time.

7. SUMMARY AND CONCLUSIONS

We have presented observations of galaxies and intergalactic gas toward the $z = 2.73$ quasar HS1700+6416, with the goal exploring the effects of galaxy formation feedback on the IGM. The unique aspect of our analysis is its careful treatment of the absorption systems—we have performed detailed line fits and full ionization simulations to determine metallicities, gas densities, sizes,

and [Si/C] relative abundances in the IGM. Our galaxy and absorber samples are still quite small and subject to the associated small-number caveats: we have considered six absorption systems identified by the presence of O VI, N V, or Mg II in a single quasar sightline, together with 14 galaxies located within $500h_{71}^{-1}$ kpc of the sightline. However, the data quality is uniformly excellent, and even in large surveys the total number of galaxies is not as important as the density of objects close to the quasar sightline ($\lesssim 40''$). The main results of our analysis may be summarized as follows:

1. Our absorption selection identifies regions of high metallicity in the IGM, with half of the six systems exhibiting near-solar values. The metal-rich systems have small absorption thickness ($\Delta L \lesssim 1$ kpc) and high gas density ($\rho/\bar{\rho} \gtrsim 100$), and are typically mixed with shock-heated O VI. The remaining systems resemble moderately overdense intergalactic filaments with slightly higher than normal chemical enrichment.
2. In regions where we could measure [Si/C] relative abundances, there are indications of a 0.1-0.5 dex silicon enhancement. This may indicate a preferential enrichment by debris from Type II supernovae.
3. Luminous galaxies are found near two of the metal-rich absorbers at identical redshift and impact parameter $\rho \lesssim 200h_{71}^{-1}$ physical kpc. The strongest absorber in the sample is associated with the closest galaxy to the QSO sightline.
4. The absorption systems most likely arise in thin sheet- or shell-like structures. This provides an efficient way to produce large absorption cross-sections for structures with small linear dimensions. If the shells form as bubbles around high redshift galaxies, then the bubbles have radii of $R \gtrsim 100$ kpc and thickness ~ 1 kpc. Roughly half of these bubbles may be associated with known luminous galaxies, while the other half may come from galaxies with either slightly lower luminosities, or different colors than current $z \sim 2.3$ samples.
5. A generic model of radiatively efficient shocks plowing into modestly overdense filaments ($\rho/\bar{\rho} \sim 10$) explains the basic observed properties of the absorption systems.
6. We see evidence for a distinct dropoff in the intergalactic gas density (traced by $N_{\text{H I}}$) at impact parameters of ~ 1 comoving Mpc from galaxies, in agreement with the results of Adelberger et al. (2005a). At this transition, the baryonic density declines from $\rho/\bar{\rho} \sim 10-100$ to values at or slightly below the mean. The galaxies appear to be embedded in intergalactic gas structures with this scale on the sky.
7. The metallicity field is strongly enhanced within $\rho \lesssim 100-200h_{71}^{-1}$ physical kpc of galaxies, which we interpret as a signature of galaxy-formation feedback. This feedback could be triggered by supernova-driven winds, or by the violent disruption of a proto-galaxy's ISM during hierarchical

mergers. At larger radii the metallicity field resembles that of the general IGM, with abundances of $[X/H] \lesssim -2$. We showed that metal-rich debris originating in galaxies could easily travel ~ 100 kpc before sweeping up enough metal-poor ambient matter to dilute into the background metallicity field.

8. Active (i.e. shock-heated and undiluted) feedback zones only comprise a few percent of the total mass of baryons in the Ly- α forest. However, they are heavily represented in the strongest C IV systems and may comprise a substantial fraction of the C IV mass in the universe. This is significant for enrichment studies at high redshift ($z \gtrsim 5$) that make use of $\Omega_{\text{C IV}}$.

It appears that star and/or galaxy formation feedback does significantly affect the properties of the IGM within $R \sim 100-200h_{71}^{-1}$ kpc of $z \sim 2.3$ galaxies. It is less clear whether the much more dilute heavy elements observed in the widespread IGM originated from these same processes. Powerful outflows are required to cover distances $\gtrsim 150$ kpc, which is somewhat uncomfortable for theoretical feedback models and observations of the Ly- α forest velocity field. Yet the correlation function between galaxies and C IV systems extends to larger scales than what we observe for our metal-rich feedback systems. This fact has been used to argue for a combination of more energetic winds at small scales and clustering at large scales (Adelberger et al. 2003, 2005a), or early chemical pollution of the biased regions where massive galaxies form (Porciani & Madau 2005; Scannapieco 2005). It remains to be seen whether these discrepancies can be resolved by better wind models, or whether the large-scale correlations simply reflect that galaxies are embedded in intergalactic structures that were pre-enriched at $z \sim 6-10$.

We are grateful to C. Steidel and team for providing us with information about galaxy redshifts near HS1700+6416 in advance of publication, and for helpful comments on a draft of the manuscript. We also thank H.W. Chen for helpful discussions. R.S. acknowledges financial support from the MIT Pappalardo Fellowship program, and from an AAS Small Research grant. W.L.W.S thanks the National Science Foundation for supporting this work under grant AST 02-06067, and M.R. also thanks the NSF for support under grant AST 00-98492. Finally, we extend our thanks to those of Hawaiian ancestry who generously share their sacred mountain for the advancement of astronomical research.

REFERENCES

- Adelberger, K. L., Shapley, A. E., Steidel, C. C., Pettini, M., Erb, D. K., & Reddy, N. A. 2005a, *ArXiv Astrophysics e-prints*
- Adelberger, K. L., Steidel, C. C., Pettini, M., Shapley, A. E., Reddy, N. A., & Erb, D. K. 2005b, *ApJ*, 619, 697
- Adelberger, K. L., Steidel, C. C., Shapley, A. E., Hunt, M. P., Erb, D. K., Reddy, N. A., & Pettini, M. 2004, *ApJ*, 607, 226
- Adelberger, K. L., Steidel, C. C., Shapley, A. E., & Pettini, M. 2003, *ApJ*, 584, 45
- Aguirre, A., Hernquist, L., Schaye, J., Katz, N., Weinberg, D. H., & Gardner, J. 2001a, *ApJ*, 561, 521
- Aguirre, A., Hernquist, L., Schaye, J., Weinberg, D. H., Katz, N., & Gardner, J. 2001b, *ApJ*, 560, 599
- Aguirre, A., Schaye, J., T., K., Theuns, T., Rauch, M., & Sargent, W. 2003, *astro-ph/0310664*
- Arnouts, S. 2004, *astro-ph/0411391*
- Barkana, R. 2004, *MNRAS*, 347, 59
- Benson, A. J., Bower, R. G., Frenk, C. S., Lacey, C. G., Baugh, C. M., & Cole, S. 2003, *ApJ*, 599, 38
- Bruscoli, M., Ferrara, A., Marri, S., Schneider, R., Maselli, A., Rollinde, E., & Aracil, B. 2003, *MNRAS*, 343, L41
- Calzetti, D., Kinney, A. L., & Storchi-Bergmann, T. 1994, *ApJ*, 429, 582
- Carswell, B., Schaye, J., & Kim, T. 2002, *ApJ*, 578, 43
- Chaffee, F. H., Foltz, C. B., Bechtold, J., & Weymann, R. J. 1986, *ApJ*, 301, 116
- Chen, H., Kennicutt, R. C., & Rauch, M. 2005, *ApJ*, 620, 703
- Chen, H., Lanzetta, K. M., & Webb, J. K. 2001, *ApJ*, 556, 158
- Chieffi, A. & Limongi, M. 2004, *ApJ*, 608, 405
- Churchill, C. W., Rigby, J. R., Charlton, J. C., & Vogt, S. S. 1999, *ApJS*, 120, 51
- Cox, T. J., Primack, J., Jonsson, P., & Somerville, R. S. 2004, *ApJ*, 607, L87
- Davé, R., Cen, R., Ostriker, J. P., Bryan, G. L., Hernquist, L., Katz, N., Weinberg, D. H., Norman, M. L., & O'Shea, B. 2001, *ApJ*, 552, 473
- Erb, D. K., Shapley, A. E., Steidel, C. C., Pettini, M., Adelberger, K. L., Hunt, M. P., Moorwood, A. F. M., & Cuby, J. 2003, *ApJ*, 591, 101
- Franx, M., Illingworth, G. D., Kelson, D. D., van Dokkum, P. G., & Tran, K. 1997, *ApJ*, 486, L75+
- Fujita, A., Mac Low, M., Ferrara, A., & Meiksin, A. 2004, *ApJ*, 613, 159
- Furlanetto, S. R. & Loeb, A. 2003, *ApJ*, 588, 18
- Gnedin, N. Y. 1998, *MNRAS*, 294, 407
- Haardt, F. & Madau, P. 1996, *ApJ*, 461, 20
- Haehnelt, M. G., Steinmetz, M., & Rauch, M. 1996, *ApJ*, 465, L95+
- Heckman, T. M., Sembach, K. R., Meurer, G. R., Strickland, D. K., Martin, C. L., Calzetti, D., & Leitherer, C. 2001, *ApJ*, 554, 1021
- Kennicutt, R. C., Bresolin, F., & Garnett, D. R. 2003, *ApJ*, 591, 801
- Kim, T.-S., Cristiani, S., & D'Odorico, S. 2001, *A&A*, 373, 757
- Kollmeier, J. A., Miralda-Escude, J., Cen, R., & Ostriker, J. P. 2005, *ArXiv Astrophysics e-prints*
- Kurk, J. D., Röttgering, H. J. A., Pentericci, L., Miley, G. K., van Breugel, W., Carilli, C. L., Ford, H., Heckman, T., McCarthy, P., & Moorwood, A. 2000, *A&A*, 358, L1
- Lanzetta, K. M. 1993, *PASP*, 105, 1063
- Lehnert, M. D. & Heckman, T. M. 1996, *ApJ*, 462, 651
- Leitherer, C., Schaerer, D., Goldader, J. D., Delgado, R. M. G., Robert, C., Kune, D. F., de Mello, D. F., Devost, D., & Heckman, T. M. 1999, *ApJS*, 123, 3
- Mac Low, M. & Ferrara, A. 1999, *ApJ*, 513, 142
- Mac Low, M. & McCray, R. 1988, *ApJ*, 324, 776
- Madau, P., Ferrara, A., & Rees, M. J. 2001, *ApJ*, 555, 92
- Martin, C. L. 1999, *ApJ*, 513, 156
- Martin, C. L., Kobulnicky, H. A., & Heckman, T. M. 2002, *ApJ*, 574, 663
- Miralda-Escudé, J. 2005, *ApJ*, 620, L91
- Miralda-Escudé, J., Cen, R., Ostriker, J. P., & Rauch, M. 1996, *ApJ*, 471, 582
- Mo, H. J. & White, S. D. M. 2002, *MNRAS*, 336, 112
- O'Meara, J. M., Tytler, D., Kirkman, D., Suzuki, N., Prochaska, J. X., Lubin, D., & Wolfe, A. M. 2001, *ApJ*, 552, 718
- Pentericci, L., Kurk, J. D., Röttgering, H. J. A., Miley, G. K., van Breugel, W., Carilli, C. L., Ford, H., Heckman, T., McCarthy, P., & Moorwood, A. 2000, *A&A*, 361, L25
- Pettini, M., Madau, P., Bolte, M., Prochaska, J. X., Ellison, S. L., & Fan, X. 2003, *ApJ*, 594, 695
- Pettini, M., Rix, S. A., Steidel, C. C., Adelberger, K. L., Hunt, M. P., & Shapley, A. E. 2002, *ApJ*, 569, 742
- Pettini, M., Shapley, A. E., Steidel, C. C., Cuby, J., Dickinson, M., Moorwood, A. F. M., Adelberger, K. L., & Giavalisco, M. 2001, *ApJ*, 554, 981
- Porciani, C. & Madau, P. 2005, *ApJ*, 625, L43
- Rauch, M., Haehnelt, M. G., & Steinmetz, M. 1997a, *ApJ*, 481, 601
- Rauch, M., Miralda-Escude, J., Sargent, W. L. W., Barlow, T. A., Weinberg, D. H., Hernquist, L., Katz, N., Cen, R., & Ostriker, J. P. 1997b, *ApJ*, 489, 7
- Rauch, M., Sargent, W. L. W., & Barlow, T. A. 2001, *ApJ*, 554, 823
- Rauch, M., Sargent, W. L. W., & Simcoe, R. A. 2005, Submitted to *ApJ*.
- Reddy, N. A., Steidel, C. C., Adelberger, K., Shapley, A., Erb, D., & Pettini, M. 2005, In Preparation
- Reimers, D., Clavel, J., Grootte, D., Engels, D., Hagen, H. J., Naylor, T., Wamsteker, W., & Hopp, U. 1989, *A&A*, 218, 71
- Reimers, D., Fechner, C., Kriss, G., Shull, M., Baade, R., Moos, W., Songaila, A., & Simcoe, R. 2004, *astro-ph/0410588*
- Rigby, J. R., Charlton, J. C., & Churchill, C. W. 2002, *ApJ*, 565, 743
- Scannapieco, E. 2005, *ApJ*, 624, L1
- Schaye, J. 2001, *ApJ*, 559, 507
- . 2004, *ArXiv Astrophysics e-prints*
- Schaye, J., Aguirre, A., Kim, T., Theuns, T., Rauch, M., & Sargent, W. L. W. 2003, *ApJ*, 596, 768
- Schaye, J., Theuns, T., Rauch, M., Efstathiou, G., & Sargent, W. L. W. 2000, *MNRAS*, 318, 817
- Scott, J., Bechtold, J., Dobrzycki, A., & Kulkarni, V. P. 2000, *ApJS*, 130, 67
- Shapley, A., Steidel, C., Erb, D., Reddy, N., Adelberger, K., Pettini, M., Barmby, P., & Huang, J. 2005, *astro-ph/0503485*
- Shapley, A. E., Erb, D. K., Pettini, M., Steidel, C. C., & Adelberger, K. L. 2004, *ApJ*, 612, 108
- Shapley, A. E., Steidel, C. C., Adelberger, K. L., Dickinson, M., Giavalisco, M., & Pettini, M. 2001, *ApJ*, 562, 95
- Simcoe, R. A., Sargent, W. L. W., & Rauch, M. 2002, *ApJ*, 578, 737
- . 2004, *ApJ*, 606, 92
- Songaila, A. 2001, *ApJ*, 561, L153
- Songaila, A. & Cowie, L. L. 1996, *AJ*, 112, 335
- Spergel, D. N., Verde, L., & Other, P. 2003, *astro-ph*
- Steidel, C., Adelberger, K., Shapley, A., Erb, D., Reddy, N., & Pettini, M. 2005, *astro-ph/0502432*
- Steidel, C. C., Adelberger, K. L., Dickinson, M., Giavalisco, M., Pettini, M., & Kellogg, M. 1998, *ApJ*, 492, 428
- Steidel, C. C., Adelberger, K. L., Giavalisco, M., Dickinson, M., & Pettini, M. 1999, *ApJ*, 519, 1
- Steidel, C. C., Shapley, A. E., Pettini, M., Adelberger, K. L., Erb, D. K., Reddy, N. A., & Hunt, M. P. 2004, *ApJ*, 604, 534
- Sutherland, R. S. & Dopita, M. A. 1993, *ApJS*, 88, 253
- Tripp, T. M., Lu, L., & Savage, B. D. 1997, *ApJS*, 112, 1
- Umeda, H. & Nomoto, K. 2002, *ApJ*, 565, 385
- Venemans, B. P., Kurk, J. D., Miley, G. K., Röttgering, H. J. A., van Breugel, W., Carilli, C. L., De Breuck, C., Ford, H., Heckman, T., McCarthy, P., & Pentericci, L. 2002, *ApJ*, 569, L11
- Vogel, S. & Reimers, D. 1995, *A&A*, 294, 377
- Weinberg, D. H., Miralda-Escude, J., Hernquist, L., & Katz, N. 1997, *ApJ*, 490, 564
- Woosley, S. E. & Weaver, T. A. 1995, *ApJS*, 101, 181

TABLE 1
 CONFIRMED AND CANDIDATE $z \sim 2 - 2.5$ GALAXIES NEAR HS1700+6416

Galaxy	$\rho(h_{71}^{-1} \text{ kpc})$	z	R	$M_{2000\text{\AA}}$	L/L^*	$\log(M_*/M_\odot)$	SFR ($M_\odot \text{ yr}^{-1}$)
MD103 [†]	115.3	2.3148	24.23	-22.09	0.81	11.07	64
MD109 [†]	208.0	2.2942	25.46	-20.84	0.26	10.48	14
BX717 [†]	216.3	2.4353	24.78	-21.66	0.49	9.85	20
BX691 [†]	290.1	2.1895	25.33	-20.84	0.29	11.04	33
BX709	316.1	2.285	25.18	-21.11	0.34	10.37	10
BX635	327.3	1.860	24.87	-20.86	0.45
MD119	336.2	2.566	25.04	-21.44	0.38
BX759	369.9	2.418	24.43	-21.99	0.67	10.52	73
MD92	431.1	2.691	25.47	-21.04	0.26
BX756	473.7	1.738	23.21	-22.34	2.07	9.76	377
BX767	409.0		24.64				
BX629	410.0		24.06				
BX720	421.9		24.74				
BX632	428.2		25.12				

[†]Redshift and SFR determined from H α emission line (Erb et al. 2003). Other objects' redshifts were determined from optical spectra (Steidel et al. 2004), and SFR from population synthesis models (Shapley et al. 2005).

TABLE 2
VOIGT PROFILE FIT COMPONENTS

Ion	z	Voigt Profile Parameters		Linewidth T		Model Params	
		b (km s $^{-1}$)	$\log N$ (cm $^{-2}$)	T_b (K)	b_{nt}	$\log N_{\text{mod}}$	T_{eq}
Voigt Profile Components: $z = 1.845$ absorption system							
Si IV	1.844840 ± 0.000002	3.14 ± 0.19	12.498 ± 0.030	$\leq 16,000$...	12.465	10,000
Si III		3.14^\dagger	12.452 ± 0.094			12.505	
Si II		3.14^\dagger	≤ 11.706			11.221	
C II		4.81^\dagger	12.631 ± 0.098			12.615	
C IV		4.81^\dagger	13.490 ± 0.023			13.492	
H I		23.00^\dagger	< 16.0			14.641	
Si IV	1.845035 ± 0.000001	3.52 ± 0.43	13.001 ± 0.061	$\leq 26,000$...	12.979	8,200
Si II		3.52^\dagger	12.592 ± 0.025			12.560	
Si III		3.52^\dagger	13.512 ± 0.156			13.369	
C II		6.09 ± 0.39	13.692 ± 0.020			13.613	
Al II		6.08 ± 1.87	11.041 ± 0.078			11.610	
Mg II		3.09 ± 0.18	12.442 ± 0.016			12.437	
H I		20.00^\dagger	< 16.5			15.580	
N V	1.845044 ± 0.000002	15.42 ± 3.50	13.421 ± 0.091	$\lesssim 200,000$	≤ 13.7	13.324	$\gtrsim 14,000$
Si IV		14.59 ± 1.16	12.951 ± 0.025			13.026	
C IV		16.11^\dagger	14.430 ± 0.007			14.472	
H I		35.0^a	$\lesssim 15.5$			14.619	
Si IV	1.845410 ± 0.000010	5.88 ± 1.34	12.413 ± 0.100	$\lesssim 60,000$	~ 0	12.427	10,000
Si III		5.88^\dagger	12.369 ± 0.036			12.376	
C IV		9.11 ± 0.83	13.669 ± 0.064			13.648	
Si IV	1.845511 ± 0.000016	4.34 ± 2.97	12.120 ± 0.183	$\lesssim 35,000$...	12.128	8,400
Si III		4.34^\dagger	12.490 ± 0.050			12.468	
C IV		7.35 ± 1.62	13.012 ± 0.267			13.031	
N V	1.845258 ± 0.000130	24.44 ± 11.95	13.091 ± 0.305				
Voigt Profile Components: $z = 2.168$ absorption system							
C IV	2.167537 ± 0.000008	12.89 ± 1.15	12.808 ± 0.030	$< 120,000$
H I		30.0^\dagger	$\lesssim 14.5$			≤ 14.5	
Si IV	2.167935 ± 0.000002	11.15^\dagger	13.159 ± 0.010	$\leq 70,000$	≥ 9.0	13.104	29,900
Si III		11.15 ± 0.21	13.021 ± 0.019			13.304	
C II		13.44^\dagger	12.989 ± 0.032			12.734	
C IV		13.44 ± 0.20	13.987 ± 0.010			13.995	
Mg II		8.21 ± 4.28	11.391 ± 0.153			11.625	
Al II		10.04 ± 9.22	10.801 ± 0.397			10.808	
H I		25.0^b	$\lesssim 16.8^b$			16.368	
Si IV	2.168064 ± 0.000003	4.90 ± 0.41	12.469 ± 0.044	$\leq 15,000$...	12.518	22,000
Si III		4.90^\dagger	13.218 ± 0.106			13.067	
C II		4.35 ± 1.59	12.331 ± 0.109			12.326	
C IV		4.35^\dagger	12.564 ± 0.171			12.763	
Mg II		3.26 ± 2.06	11.401 ± 0.113			11.599	
Al II		23.32 ± 18.26	10.956 ± 0.391			10.804	
H I		25.0^b	$\leq 16.2^b$			16.246	
H I	2.168938 ± 0.000009	25.58 ± 0.80	13.870 ± 0.016				
Voigt Profile Components: $z = 2.315$ absorption system							
C IV	2.313843 ± 0.000012	8.14 ± 0.15	12.392 ± 0.081	$< 47,000$...	12.392	6600
H I		28.10^\dagger	14.225 ± 0.028			14.214	
Si II	2.314895 ± 0.000016	7.52 ± 1.03	12.660 ± 0.086	$\leq 90,000$	≥ 0	12.580	5400
N II		10.64^\dagger	12.592 ± 0.120			12.585	
Al II		7.67^\dagger	11.116 ± 0.108			11.390	
Mg II		8.00^\dagger	12.324 ± 0.091			12.292	
C II		11.50^\dagger	13.420 ± 0.105			13.350	
Si II	2.314996 ± 0.000002	3.31 ± 0.32	12.831 ± 0.058	$\leq 18,000$	> 0	12.825	≤ 5400
N II		4.68^\dagger	12.724 ± 0.069			12.882	
Al II		3.38^\dagger	11.261 ± 0.073			11.463	
Fe II		2.35^\dagger	11.606 ± 0.106			12.001	
Mg II		3.56^\dagger	12.705 ± 0.036			12.716	
C II		5.06^\dagger	13.648 ± 0.061			13.436	
H I		18.51^\dagger	$15.5 \lesssim N_{\text{H I}} \lesssim 16.862$			15.576	
Si II	2.315504 ± 0.000001	3.01 ± 0.09	12.943 ± 0.022	$\leq 15,000$	> 0	12.858	≤ 5400
N II		4.25^\dagger	13.107 ± 0.027			13.150	
C II		4.60^\dagger	13.643 ± 0.008			13.687	
Mg II		3.23^\dagger	12.579 ± 0.019			12.653	
Fe II		2.13^\dagger	12.119 ± 0.025			12.338	
Al II		3.07^\dagger	11.463 ± 0.045			11.727	
H I		15.90^\dagger	$14.939 \leq N_{\text{H I}} \lesssim 17.0$			15.569	
Si IV	2.316350 ± 0.000001	4.08 ± 0.06	12.963 ± 0.005	16,600	2.6	12.977	18,000
C IV		5.46 ± 1.77	13.944 ± 0.160			14.295	
N V		8.12 ± 0.69	13.198 ± 0.024			12.997	

TABLE 2 — *Continued*

Ion	z	Voigt Profile Parameters		Linewidth T		Model Params	
		b (km s $^{-1}$)	$\log N$ (cm $^{-2}$)	T_b (K)	b_{nt}	$\log N_{\text{mod}}$	T_{eq}
H I		21.75 †	≤ 14.3			14.127	
Si IV	2.314470 ± 0.000007	5.19 ± 0.78	11.853 ± 0.065	$\leq 45,000$...	11.842	11,000
C IV		7.93 †	13.057 ± 0.048			13.068	
H I		27.5 †	≤ 14.7			13.126	
O VI	2.314992 ± 0.000019	11.90 †	13.951 ± 0.108	$\gtrsim 230,000$
N V		12.72 ± 1.41	≤ 13.043				
O VI	2.315182 ± 0.000012	11.64 †	14.259 ± 0.054	$\gtrsim 250,000$
N V		12.44 ± 1.18	≤ 13.026				
Si IV	2.314900 ± 0.000005	7.45 ± 0.26	13.550 ± 0.036	$\lesssim 43,000$	$\gtrsim 5.5$	13.526	8300
C IV		9.46 ± 0.48	14.309 ± 0.042			14.295	
N V		10.75 ± 4.84	12.741 ± 0.152			12.782	
H I		32.77 †	$\lesssim 15.4$			15.094	
N V	2.315117 ± 0.000007	11.97 ± 1.68	13.154 ± 0.054	$< 70,000$	> 0	13.163	12,000
C IV		10.00 ± 0.96	14.391 ± 0.047			14.381	
Si IV			≤ 13.1			13.010	
H I		34.6 †	$\gtrsim 16.1$			14.286	
N V	2.315556 ± 0.000010	22.57 ± 2.38	13.186 ± 0.050	13.137	14,000
C IV		24.38 †	14.420 ± 0.030			14.370	
Si IV		24.38 †	≤ 12.856			12.976	
H I		30.0 †	$\gtrsim 15.7$			14.536	
C IV	2.315868 ± 0.000003	7.52 ± 0.77	13.923 ± 0.062	$\leq 40,000$...	13.932	15,500
N V		6.96 †	12.801 ± 0.074			12.787	
Si IV		4.91 †	12.387 ± 0.031			12.392	
H I		26.0 †	≤ 15.0			13.972	
N V	2.316071 ± 0.000004	5.28 ± 0.93	12.539 ± 0.088	$\leq 23,000$...	12.378	12,500
C IV		5.70 †	13.248 ± 0.057			13.514	
Si IV		3.73 †	12.002 ± 0.043			11.998	
H I		20.0 †	≤ 14.7			13.289	
O VI	2.315790 ± 0.000014	34.43 ± 2.14	14.675 ± 0.021			...	$\gtrsim 250,000$
N V		31.87 †	≤ 13.415				
O VI	2.316345 ± 0.000011	13.20 ± 1.53	14.068 ± 0.065			...	$\gtrsim 230,000$
N V		12.22 †	≤ 13.261				
O VI	2.316693 ± 0.000063	45.16 ± 4.91	14.087 ± 0.065			...	$\gtrsim 260,000$
N V		41.81 †	≤ 12.632				
O VI	2.314618 ± 0.000068	46.80 ± 14.92	13.829 ± 0.125			...	$\gtrsim 260,000$
N V		43.30 †	≤ 12.612				
C IV	2.315455 ± 0.000011	1.06 ± 4.64	13.517 ± 5.127			...	
C IV	2.316317 ± 0.000013	8.97 ± 0.44	14.074 ± 0.170			...	
C IV	2.316587 ± 0.000011	6.14 ± 1.49	12.625 ± 0.075			...	
Si IV	2.315501 ± 0.000003	2.00 ± 1.39	12.938 ± 0.088			...	
Si IV	2.314995 ± 0.000003	2.76 ± 0.79	13.427 ± 0.105			...	
Si IV	2.315128 ± 0.000003	6.11 ± 0.79	13.069 ± 0.053			...	
Si IV	2.315395 ± 0.000076	13.75 ± 6.60	13.106 ± 0.326			...	
Si IV	2.315578 ± 0.000078	8.93 ± 7.47	12.856 ± 0.695			...	
Si IV	2.315757 ± 0.000007	2.25 ± 1.99	12.172 ± 0.152			...	
Voigt Profile Components: $z = 2.379$ absorption system							
C IV	2.379919 ± 0.000002	9.92 ± 0.26	13.056 ± 0.008	50,000	5.24	13.043	29,000
C III		9.92 †	13.363 ± 0.088			13.430	
Si III		7.61 ± 0.71	11.755 ± 0.032			11.874	
Si IV		7.61 †	11.788 ± 0.039			11.657	
Si II		7.61 †	≤ 11.610			10.697	
H I		23.84 ± 0.69	15.393 ± 0.057			15.490	
O VI	2.379988 ± 0.000009	19.57 ± 1.12	13.518 ± 0.021	$\leq 370,000$	$\gtrsim 280,000$
N V		18.1 †	≤ 12.005				
H I	2.379291 ± 0.000057	50.00 ± 2.61	14.487 ± 0.065				
H I	2.380634 ± 0.000047	26.20 ± 3.52	13.098 ± 0.088				
Voigt Profile Components: $z = 2.43$ absorption system							
C II	2.433052 ± 0.000001	7.37 †	12.756 ± 0.049	17,500	5.48	12.655	19,700
C III		7.37 †	13.884 ± 0.516			13.887	
C IV		7.37 ± 0.66	12.940 ± 0.133			12.967	
Si II		6.36 †	12.129 ± 0.042			12.018	
Si III		6.36 †	13.134 ± 0.018			13.156	
Si IV		6.36 †	12.582 ± 0.018			12.580	
Al II		6.44 †	10.941 ± 0.072			11.187	
H I		17.92 †	15.751 ± 0.250			15.887	
C II	2.433426 ± 0.000008	16.74 †	12.726 ± 0.053	$\leq 60,000$	13.95	12.627	19,700
C IV		16.74 ± 2.46	12.650 ± 0.234			12.939	
Si II		15.21 †	11.975 ± 0.025			11.864	
Si III		15.21 ± 0.84	12.891 ± 0.027			13.003	

TABLE 2 — *Continued*

Ion	z	Voigt Profile Parameters		Linewidth T		Model Params	
		b (km s $^{-1}$)	$\log N$ (cm $^{-2}$)	T_b (K)	b_{nt}	$\log N_{\text{mod}}$	T_{eq}
Si IV		15.21 †	12.495 \pm 0.040			12.427	
H I		34.95 †	15.719 \pm 0.354			15.859	
C II	2.433650 \pm 0.000001	10.54 †	12.446 \pm 0.071	\leq 55,000	\geq 5.93	12.338	19,700
C IV		10.54 \pm 0.84	12.643 \pm 0.050			12.650	
Si II		8.23 †	11.371 \pm 0.071			11.626	
Si III		8.23 \pm 0.72	12.751 \pm 0.048			12.764	
Al II		8.54 †	10.758 \pm 0.094			10.870	
H I		30.76 †	15.641 \pm 0.153			15.570	
C IV	2.431814 \pm 0.000012	7.22 \pm 1.78	12.273 \pm 0.123	12.162	35,000
C III		7.22 †	12.145 \pm 0.228			12.294	
H I		25.01 †	15.055 \pm 0.022			14.861	
C IV	2.432091 \pm 0.000015	18.20 †	12.841 \pm 0.041	12.818	31,800
C III		18.20 \pm 2.05	12.998 \pm 0.047			13.023	
H I		29.84 \pm 1.20	15.401 \pm 0.069			15.370	
C IV	2.432632 \pm 0.000017	11.82 \pm 1.84	12.535 \pm 0.074		
C III		11.82 †	12.970 \pm 0.070				
Si IV		50.00 \pm 37.76	12.076 \pm 0.278				
C IV	2.432933 \pm 0.000026	10.97 \pm 2.71	12.927 \pm 0.139	12.882	24,000
C III		10.97 †	13.227 \pm 0.181			13.504	
C II		10.97 †	12.183 \pm 0.168			12.048	
H I		26.01 \pm 5.88	15.567 \pm 0.147			15.423	
O VI	2.432600 \pm 0.000145	42.97 \pm 12.70	13.467 \pm 0.164	\leq 1,700,000	\gtrsim 224,000
N V		42.97 †	12.788 \pm 0.082				
O VI	2.433233 \pm 0.000030	26.64 \pm 5.63	13.590 \pm 0.141	\leq 680,000	\gtrsim 280,000
N V		26.60 †	\leq 12.030				
O VI	2.433749 \pm 0.000037	18.15 \pm 3.72	13.158 \pm 0.116	\leq 316,000	\gtrsim 280,000
N V		18.15 †	11.531 \pm 0.213				
C IV	2.433285 \pm 0.000021	13.86 \pm 3.59	12.876 \pm 0.160				
C II	2.438637 \pm 0.000003	10.92 \pm 0.49	12.001 \pm 0.094	\leq 85,000	...	11.872	28,500
C III		10.92 †	13.492 \pm 0.052			13.458	
C IV		10.92 †	13.079 \pm 0.016			13.080	
Si II		7.14 †	\leq 11.500				
Si III		7.14 †	12.111 \pm 0.032			12.218	
Si IV		7.14 †	12.259 \pm 0.025			12.430	
H I		37.83 †	15.510 \pm 0.035			15.405	
C II	2.438857 \pm 0.000002	6.55 \pm 0.46	11.946 \pm 0.087	21,000	3.75	12.064	22,000
C III		6.55 †	13.626 \pm 0.126			13.517	
C IV		6.55 †	12.848 \pm 0.022			12.864	
Si II		5.14 †	\leq 11.577				
Si III		5.14 \pm 0.41	12.248 \pm 0.040			12.452	
Si IV		5.14 †	12.200 \pm 0.025			12.065	
H I		19.00 †	15.316 \pm 0.084			15.240	
Si III	2.438286 \pm 0.000006	21.61 \pm 2.28	12.147 \pm 0.034	\leq 100,000	...	12.173	31,800
Si IV		21.61 †	12.021 \pm 0.062			12.022	
C III		11.17 †	12.963 \pm 0.041			12.952	
C IV		11.17 \pm 0.86	12.671 \pm 0.028			12.656	
H I		13.15 \pm 0.96	15.221 \pm 0.089			15.086	
C III	2.437774 \pm 0.000004	8.53 \pm 0.55	12.835 \pm 0.043	\leq 52,000	...	12.796	27,000
C IV		8.53 †	12.682 \pm 0.022			12.636	
Si III		5.58 †	11.196 \pm 0.111			11.321	
Si IV		5.58 †	11.331 \pm 0.112			11.310	
H I		31.75 \pm 0.52	13.992 \pm 0.014			13.960	
C IV	2.440517 \pm 0.000005	9.80 \pm 0.54	13.080 \pm 0.028	\leq 70,000	...	12.782	27,000
Si IV		9.80 †	\leq 11.596			11.422	
H I		34.08 †	14.558 \pm 0.022			14.536	
O VI	2.439748 \pm 0.000013	14.8 \pm 1.86	13.570 \pm 0.044	\lesssim 210,000	\gtrsim 234,000
N V		14.8 †	\leq 12.533				
O VI	2.440253 \pm 0.000032	15.96 \pm 3.90	13.492 \pm 0.137	\lesssim 245,000	\gtrsim 240,000
N V		15.96 †	\leq 12.407				
O VI	2.440560 \pm 0.000014	9.76 \pm 3.10	13.370 \pm 0.273	\lesssim 91,000	\gtrsim 230,000
N V		9.76 †	\leq 12.450				
O VI	2.440737 \pm 0.000147	26.79 \pm 9.20	13.559 \pm 0.262	\leq 690,000	\sim 224,000
N V		26.79 †	12.828 \pm 0.081				
O VI	2.437790 \pm 0.000062	23.58 \pm 5.75	13.238 \pm 0.126	\leq 535,000	\sim 230,000
N V		23.58 †	12.389 \pm 0.068				
O VI	2.438248 \pm 0.000040	20.14 \pm 5.46	13.250 \pm 0.158	\leq 390,000	\sim 240,000
N V		20.14 †	12.185 \pm 0.077				
O VI	2.438963 \pm 0.000020	36.57 \pm 3.59	13.827 \pm 0.035	$<$ 1,285,000	\sim 270,000
N V		36.57 †	12.338 \pm 0.162				

TABLE 2 — *Continued*

Ion	z	Voigt Profile Parameters		Linewidth T		Model Params	
		b (km s $^{-1}$)	$\log N$ (cm $^{-2}$)	T_b (K)	b_{nt}	$\log N_{\text{mod}}$	T_{eq}
C IV	2.439829 ± 0.000041	50.00 ± 6.16	12.893 ± 0.042				
C IV	2.440775 ± 0.000014	12.50 ± 1.55	12.782 ± 0.048				
Si III	2.437852 ± 0.000024	10.97 ± 3.30	11.401 ± 0.117				
Si III	2.438954 ± 0.000039	17.29 ± 2.60	11.934 ± 0.110				
Voigt Profile Components: $z = 2.578$ absorption system							
C IV	2.578167 ± 0.000007	25.64 ± 0.97	13.340 ± 0.014	$\leq 350,000$	≥ 13.26	13.332	27,600
C III		25.64^\dagger	13.275 ± 0.018			13.270	
Si IV		19.55 ± 12.37	11.671 ± 0.213			11.685	
H I		29.06 ± 0.22	$\lesssim 15.3$			14.276	
C IV	2.578870 ± 0.000004	22.30 ± 0.67	13.177 ± 0.014	$\leq 350,000$...	13.112	26,500
C III		22.30^\dagger	13.458 ± 0.014			13.457	
Si IV		14.58^\dagger	11.883 ± 0.091			11.960	
H I		29.06 ± 0.22	15.642 ± 0.014			15.485	
O VI	2.578121 ± 0.000054	22.86 ± 2.47	13.669 ± 0.223	$\leq 500,000$	$\gtrsim 230,000$
N V		24.43^\dagger	12.749 ± 0.186				
O VI	2.578495 ± 0.000071	28.90 ± 4.29	13.930 ± 0.124	$\leq 800,000$	$\gtrsim 250,000$
N V		30.89^\dagger	12.851 ± 0.158				
O VI	2.579176 ± 0.000022	9.51 ± 3.05	12.640 ± 0.115				
H I	2.575657 ± 0.000026	8.20 ± 4.58	11.718 ± 0.254				
H I	2.575862 ± 0.000034	34.67 ± 3.04	12.688 ± 0.037				
H I	2.577126 ± 0.000028	38.66 ± 2.07	13.560 ± 0.033				
H I	2.577974 ± 0.000005	26.29 ± 0.33	15.568 ± 0.014				
H I	2.580563 ± 0.000006	33.14 ± 0.65	13.198 ± 0.007				

TABLE 3
BEST-FIT CLOUDY MODEL PARAMETERS

z	Fit Parameters			Derived Parameters			Line Constraints
	[X/H]	$\log(n_H)$	[Si/C]	ΔL (pc) ¹	$\log(N_{H\text{ I}})$	T (K)	
1.844840	$0.00^{+0.5}_{-0.5}$	$-2.60^{+0.1}_{-0.1}$	$-0.3^{+0.2}_{-0.2}$	64^{+113}_{-48}	$14.641^{+0.4}_{-0.6}$	9500^{+6500}_{-700}	H I [†] , C II, C IV, Si II [†] , Si III, Si IV
1.845035	$0.00^{+0.5}_{-0.5}$	$-2.25^{+0.15}_{-0.10}$	$-0.2^{+0.1}_{-0.1}$	104^{+63}_{-83}	$15.581^{+0.5}_{-0.5}$	8100^{+7000}_{-200}	H I [†] , C II, Si II, Si III, Si IV, Mg II, Al II
1.845044	$0.00^{+0.5}_{-1.0}$	$-3.20^{+0.2}_{-0.2}$...	1208^{+12000}_{-850}	$14.619^{+1.1}_{-0.3}$	$13,800^{+13,000}_{-1000}$	H I [†] , N V, C IV, Si IV
1.845410	0.00^a	$-2.70^{+0.2}_{-0.2}$	$-0.4^{+0.5}_{-0.5}$	96^{+100}_{-60}	$14.607^{+0.6}_{-0.6}$	$10,100^{+1000}_{-500}$	C IV, Si III, Si IV
1.845511	0.00^a	$-2.30^{+0.3}_{-0.3}$	$-0.4^{+0.4}_{-0.5}$	24^{+100}_{-10}	$14.844^{+0.7}_{-0.4}$	8400^{+1100}_{-800}	C IV, Si III, Si IV
2.167935	$-2.00^{+1.5}_{-0.5}$	$-2.95^{+0.35}_{-0.0}$	$0.6^{+0.1}_{-0.4}$	39109^{+17052}_{-38582}	$16.368^{+0.37}_{-1.2}$	$29,900^{+0}_{-10,000}$	H I [†] , C II, C IV, Si III, Si IV, Mg II, Al II
2.168064	$-2.25^{+0.75}_{-0.25}$	$-2.00^{+0.1}_{-0.35}$	$0.6^{+0.1}_{-0.3}$	898^{+598}_{-520}	$16.246^{+0.3}_{-0.6}$	$22,000^{+3500}_{-2000}$	H I [†] , C II, C IV, Si III, Si IV, Mg II, Al II
2.314470	$0.00^{+0.5}_{-1.2}$	$-3.00^{+0.35}_{-0}$...	32^{+475}_{-24}	$13.127^{+1.60}_{-0.45}$	$11,000^{+12,700}_{-1000}$	H I [†] , C IV, Si IV
2.314895	$0.00^{+0.25}_{-0.25}$	$-1.50^{+0.30}_{-0.40}$	$0.0^{+0.1}_{-0.2}$	$2.0^{+1.0}_{-1.3}$	$15.084^{+0.25}_{-0.70}$	5400^{+6500}_{-400}	N II, Al II, Mg II, C II, Si II
2.314996	$-0.25^{+0.25}_{-0.75}$	$-1.00^{+0.2}_{-0.25}$	$0.3^{+0.1}_{-0.3}$	$0.7^{+0.3}_{-0.1}$	$15.576^{+0.25}_{-0.25}$	$\gtrsim 5400$	H I [†] , N II, Al II, Mg II, C II, Si II, Fe II
2.315504	$0.00^{+0.5}_{-0.5}$	$-1.00^{+0.15}_{-0.0}$	$0.0^{+0.1}_{-0.1}$	$0.6^{+0.68}_{-0.40}$	$15.569^{+0.544}_{-0.459}$	$\gtrsim 5400$	H I [†] , N II, Al II, Mg II, C II, Si II, Fe II
2.316350	$0.25^{+0.25}_{-0.5}$	$-2.90^{+0.00}_{-0.2}$...	292^{+773}_{-99}	$14.128^{+0.328}_{-0.428}$	$18,000^{+1000}_{-8000}$	H I [†] , C IV, Si IV, N v
2.314992	$\gtrsim 230,000$	O VI, N v [†]
2.315182	$\gtrsim 250,000$	O VI, N v [†]
2.315790	$\gtrsim 250,000$	O VI, N v [†]
2.316345	$\gtrsim 230,000$	O VI, N v [†]
2.316693	$\gtrsim 260,000$	O VI, N v [†]
2.314618	$\gtrsim 260,000$	O VI, N v [†]
2.314900	$0.00^{+0.5}_{-0.25}$	$-2.60^{+0.25}_{-0.0}$...	405^{+230}_{-297}	$15.094^{+0.321}_{-0.360}$	8300^{+7200}_{-1300}	C IV, N v, Si IV, H I [†]
2.315117	$0.00^{+0.5}_{-2}$	$-3.10^{+0.15}_{-0.0}$...	$784^{+113,000}_{-545}$	$14.286^{+2}_{-0.567}$	$12,000^{+22,000}_{-1000}$	C IV, N v, Si IV [†] , H I [†]
2.316071	$0.00^{+0.5}_{-1.0}$	$-3.20^{+0.2}_{-0.2}$...	130^{+235}_{-89}	$13.290^{+1.213}_{-0.73}$	$12,500^{+15,000}_{-1500}$	C IV, N v, Si IV, H I [†]
2.315868	$-0.25^{+0.75}_{-0.75}$	$-3.15^{+0.15}_{-0.05}$...	574^{+2842}_{-470}	$13.972^{+0.929}_{-0.748}$	$15,500^{+10,000}_{-5500}$	C IV, N v, Si IV, H I [†]
2.315556	$-0.25^{+0.75}_{-1.0}$	$-3.05^{+0.1}_{-0.05}$...	$1280^{+17,600}_{-1048}$	$14.536^{+1.164}_{-0.756}$	$14,000^{+10,000}_{-4000}$	C IV, N v, Si IV [†] , H I [†]
2.313843	$0.0^{+0.1}_{-0.1}$	$-2.15^{+0.1}_{-0.1}$...	6^{+3}_{-3}	$14.214^{+0.100}_{-0.100}$	6600^{+6500}_{-300}	C IV, H I
2.379919	$-2.0^{+0.2}_{-0.2}$	$-3.05^{+0.2}_{-0.3}$	$0.3^{+0.3}_{-0.3}$	5448^{+2000}_{-2000}	$15.294^{+0.2}_{-0.1}$	$29,000^{+2000}_{-2000}$	H I, C III, C IV, Si III, Si IV, Si II [†]
2.379988	$\gtrsim 280,000^*$	O VI, N v [†]
2.431814	$-2.75^{+0.25}_{-0.25}$	$-2.85^{+0.2}_{-0.3}$...	$2659^{+10,350}_{-1850}$	$14.861^{+0.144}_{-0.070}$	$35,000^{+3000}_{-3000}$	H I, C III, C IV
2.432091	$-2.5^{+0.25}_{-0.25}$	$-2.75^{+0.2}_{-0.25}$...	$5105^{+10,000}_{-3000}$	$15.370^{+0.150}_{-0.163}$	$31,800^{+3000}_{-2100}$	H I, C III, C IV
2.432933	$-1.75^{+0.75}_{-0.5}$	$-2.25^{+0.25}_{-0.45}$...	450^{+2203}_{-354}	$15.423^{+0.319}_{-0.437}$	$24,000^{+7800}_{-7000}$	H I, C II, C III, C IV
2.433052	$-1.5^{+0.5}_{-0.25}$	$-1.90^{+0.20}_{-0.35}$	$0.37^{+0.15}_{-0.15}$	232^{+433}_{-110}	$15.888^{+0.38}_{-0.38}$	$19,700^{+3300}_{-4700}$	H I, C II, C III, C IV, Si II, Si III, Si IV, Al II
2.433426	$-1.5^{+0.5}_{-0.25}$	$-1.90^{+0.30}_{-0.35}$	$0.25^{+0.30}_{-0.25}$	218^{+460}_{-87}	$15.859^{+0.15}_{-0.42}$	$19,700^{+3300}_{-4700}$	H I, C II, C IV, Si II, Si III, Si IV
2.433650	$-1.5^{+0.3}_{-0.5}$	$-1.90^{+0.1}_{-0.45}$	$0.30^{+0.2}_{-0.3}$	112^{+780}_{-20}	$15.570^{+0.32}_{-0.24}$	$19,700^{+4800}_{-2700}$	H I [†] , C II, C IV, Si III, Si IV, Al II
2.432600	$\gtrsim 224,000$	O VI, N v [†]
2.433233	$\gtrsim 280,000$	O VI, N v [†]
2.433749	$\gtrsim 280,000$	O VI, N v [†]
2.437774	$-1.25^{+0.25}_{-0.25}$	$-2.75^{+0.1}_{-0.2}$	$0.4^{+0.5}_{-0.4}$	168^{+630}_{-14}	$13.961^{+0.121}_{-0.061}$	$27,000^{+3000}_{-6000}$	H I, C III, C IV, Si III, Si IV
2.438286	$-2.25^{+0.25}_{-0.25}$	$-2.65^{+0.10}_{-0.25}$	$0.20^{+0.1}_{-0.3}$	1596^{+1655}_{-50}	$15.086^{+0.363}_{-0.125}$	$31,800^{+2300}_{-7500}$	H I, C II, C III, C IV, Si II, Si III, Si IV
2.438637	$-2.0^{+0.25}_{-0.25}$	$-2.90^{+0.2}_{-0.05}$	$0.60^{+0.2}_{-0.25}$	4413^{+327}_{-3758}	$15.510^{+0.142}_{-0.098}$	$28,500^{+8500}_{-6000}$	H I, C II, C III, C IV, Si II, Si III, Si IV
2.438857	$-1.5^{+0.25}_{-0.5}$	$-2.20^{+0.15}_{-0.5}$	$0.20^{+0.3}_{-0.2}$	225^{+1850}_{-75}	$15.240^{+0.26}_{-0.24}$	$22,000^{+8000}_{-3500}$	H I, C II, C III, C IV, Si II, Si III, Si IV
2.440517	$-1.5^{+0.25}_{-0.5}$	$-2.60^{+0.2}_{-0.7}$	$0.0^{+0.8}_{-0.0}$	323^{+7500}_{-198}	$14.536^{+0.100}_{-0.100}$	$27,000^{+12,000}_{-4800}$	H I, C IV, Si IV [†]
2.439748	$\gtrsim 234,000$	O VI, N v [†]
2.440253	$\gtrsim 240,000$	O VI, N v [†]
2.440560	$\gtrsim 230,000$	O VI, N v [†]
2.440737	$\gtrsim 224,000$	O VI, N v [†]
2.437790	$\gtrsim 230,000$	O VI, N v [†]
2.438248	$\gtrsim 240,000$	O VI, N v [†]
2.438963	$\gtrsim 270,000$	O VI, N v [†]
2.578121	$\gtrsim 230,000^*$	O VI, N v
2.578167	$-1.0^{+0.75}_{-1.0}$	$-3.35^{+0.15}_{-0.1}$	$0.4^{+0.4}_{-0.4}$	$1878^{+35,000}_{-1700}$	$14.276^{+1.0}_{-0.6}$	$27,600^{+12,000}_{-10,000}$	H I [†] , C IV, C III, Si IV
2.578495	$\gtrsim 250,000^*$	O VI, N v
2.578870	$-2.0^{+0.1}_{-0.1}$	$-2.95^{+0.1}_{-0.1}$	$0.3^{+0.2}_{-0.3}$	5122^{+1000}_{-1000}	$15.485^{+0.15}_{-0.1}$	$26,500^{+2000}_{-2000}$	H I, C IV, C III, Si IV

¹ Line of sight distance through absorbing shell, averaged for all heavy element line measurements. Uses best-fit [X/H], $\log n_H$, and the CLOUDY ionization fractions that correspond to these parameters.

[†] Upper limit

* Alternate solution is available with $L \lesssim 100$ kpc, $\log n_H \sim -4$, $[X/H] \gtrsim -1.5$, photoionized.

^a Denotes systems where an accurate metallicity could not be measured because of confusion and/or blending in the H I profile. For these cases, we assume the metallicity matches other, measured components in the same complex with similar heavy element ion ratios.